UNIVERSIDAD DE INVESTIGACIÓN DE TECNOLOGÍA EXPERIMENTAL YACHAY

Escuela de Ciencias de la Tierra, Energía y Ambiente

TÍTULO: MINERALOGICAL CHARACTERIZATION OF SANDS FROM THE COTACACHI-CUICOCHA VOLCANIC COMPLEX

Trabajo de integración curricular presentado como requisito para la obtención del título de Geólogo

Autor:

Guiz Chapi Evelyn Zulay

Tutor:

M.Sc. Rodríguez Calvopiña Mariela Fernanda

Co-Tutor:

Ph.D. Vázquez Taset Yaniel Misael

Urcuquí, febrero 2024

AUTORÍA

Yo, **GUIZ CHAPI EVELYN ZULAY**, con cédula de identidad 0401861364, declaro que las ideas, juicios, valoraciones, interpretaciones, consultas bibliográficas, definiciones y conceptualizaciones expuestas en el presente trabajo; así cómo, los procedimientos y herramientas utilizadas en la investigación, son de absoluta responsabilidad de la autora del trabajo de integración curricular. Así mismo, me acojo a los reglamentos internos de la Universidad de Investigación de Tecnología Experimental Yachay.

Urcuquí, febrero 2024.

_____

Evelyn Zulay Guiz Chapi

CI: 0401861364

AUTORIZACIÓN DE PUBLICACIÓN

Yo, **GUIZ CHAPI EVELYN ZULAY**, con cédula de identidad 0401861364, cedo a la Universidad de Investigación de Tecnología Experimental Yachay, los derechos de publicación de la presente obra, sin que deba haber un reconocimiento económico por este concepto. Declaro además que el texto del presente trabajo de titulación no podrá ser cedido a ninguna empresa editorial para su publicación u otros fines, sin contar previamente con la autorización escrita de la Universidad.

Asimismo, autorizo a la Universidad que realice la digitalización y publicación de este trabajo de integración curricular en el repositorio virtual, de conformidad a lo dispuesto en el Art. 144 de la Ley Orgánica de Educación Superior

Urcuquí, febrero 2024.

_____

Evelyn Zulay Guiz Chapi

CI: 0401861364

DEDICATORY

I dedicate this work to my mom, Martha, my dad, José, and my brother, Johnny. Thanks to them for all their support and unconditional love.

Eve

ACKNOWLEDGMENTS

RESUMEN

Este estudio presenta los resultados obtenidos de la caracterización de las arenas asociadas al Complejo Volcánico Cotacachi-Cuicocha (CVCC), sus posibles aplicaciones y la identificación de Elementos de Tierras Raras (ETR). El complejo volcánico forma parte de la Cordillera Occidental del Ecuador y constituye uno de los geositios más importantes de Imbabura Geoparque Mundial de la UNESCO. El complejo se considera potencialmente activo y consta de un estratovolcán principal (Cotacachi), cuatro domos satélites (Muyurcu, Loma Negra, Peribuela, and Cuicocha), y una caldera volcánica (Cuicocha) que ha dado lugar a la formación de una laguna con dos islotes en su interior (Yerovi and Wolf). Asociado a estas geoformas, se ha desarrollado un sistema fluvial de forma radial, que drena el agua desde las partes altas del complejo volcánico, acarreando sedimentos de varios tamaños, pertenecientes a las diferentes unidades litológicas del CVCC. Siendo los cursos fluviales la fuente de obtención de 22 muestras de arenas estudiadas en este trabajo, las mismas que fueron sometidas a varios procesos físicos, análisis granulométrico, separación magnética, observaciones mediante el uso del estereomicroscopio, y técnicas analíticas como espectrometría de difracción de rayos X (DRX), espectrometría Raman y espectroscopia de fotoelectrones de rayos X (XPS). El análisis granulométrico permitió determinar que la fracción más representativa de cada muestra corresponde a los sedimentos retenidos en la malla 120 (0.025-0.125 mm) que contiene mayor porcentaje en peso de la muestra y menor cantidad de líticos. Así, con el uso de los métodos analíticos se pudo determinar que las arenas fluviales asociadas al CVCC presenta una composición mineralógica constituida principalmente por óxidos de hierro (magnetita y hematites) en un 59,05%, plagioclasa (labradorita y andesina) en un 27,55%, y piroxenos (enstatita y augita), y anfíbol (hornblenda) en un 13,40%. Sin embargo, fue imposible confirmar la presencia de ETR. De los minerales identificados, óxidos de hierro son los más representativos con respecto a su masa, donde sus nanopartículas son ampliamente utilizadas en diferentes áreas; sin embargo, el designarles una aplicación a los óxidos de hierro identificados en el CVCC conlleva un análisis de su calidad y el volumen de material disponible en la zona.

Palabras Clave: *Complejo Volcánico Cotacachi-Cuicocha, caracterización mineralógica, técnicas analíticas, sedimentos fluviales, minerales pesados, elementos de tierras raras.*

ABSTRACT

This study presents the results obtained from the characterization of the sands associated with the Cotacachi-Cuicocha Volcanic Complex (CCVC), their possible applications and the identification of Rare Earth Elements (REEs). The volcanic complex is part of the Cordillera Occidental of Ecuador and is one of the most important geosites of Imbabura UNESCO Global Geopark. The complex is considered potentially active and consists of a main stratovolcano (Cotacachi), four satellite domes (Muyurcu, Loma Negra, Peribuela, and Cuicocha), and a volcanic caldera (Cuicocha) that has led to the formation of a lake with two islets inside (Yerovi and Wolf). Associated with these geoforms, a radial fluvial system has developed, which drains water from the upper parts of the volcanic complex, carrying sediments of various sizes belonging to the different lithological units of the CCVC. The fluvial courses were the source of 22 sand samples studied in this work, which were subjected to various physical processes, granulometric analysis, magnetic separation, observations using the stereomicroscope, and analytical techniques such as X-ray diffraction spectrometry (XRD), Raman spectrometry and X-ray photoelectron spectroscopy (XPS). The granulometric analysis allowed determining that the most representative fraction of each sample corresponds to the sediments retained in the 120 mesh (0.025-0.125 mm), which contains a higher percentage by weight of the sample and a lower amount of lithics. Thus, using analytical methods, it was possible to determine that the fluvial sands associated with the CCVC have a mineralogical composition constituted mainly of iron oxides (magnetite and hematite) at 59.05%, plagioclase (labradorite and andesine) at 27.55%, and pyroxenes (enstatite and augite), and amphibole (hornblende) at 13.40%. However, it was impossible to confirm the presence of REEs. Among the detected minerals, iron oxides are the most representative with respect to their mass, where their nanoparticles are widely used in different areas; however, designating an application to the iron oxides identified in the CCVC entails an analysis of their quality and the volume of material available in the area.

Key Words: *Cotacachi-Cuicocha Volcanic Complex, mineralogical characterization, analytic techniques, fluvial sediments, heavy mineral, rare earth elements.*

INDEX

CHAPTER 1: INTRODUCTION

The Cotacachi-Cuicocha Volcanic Complex (Figure 1) is one of the most important geosites of the Imbabura UNESCO Global Geopark. It is located 10 kilometers from Cotacachi and 13 kilometers from Otavalo (Jácome et al., 2020). This complex comprises a series of geoformologies created mainly by several eruptive processes, including the Cotacachi volcano, the Cuicocha crater, and the domes Peribuela, Muyurcu, Loma Negra, and Cuicocha (Almeida, 2016). Additionally, associated with this complex, the Cuicocha crater lake developed, being the youngest eruptive center of the CCVC (Sierra et al., 2021). Along with the Quilotoa lake, this is regarded as one of Ecuador's two only caldera lakes (Jácome et al., 2020), within which there are two islets, Yerovi and Teodoro Wolf. Therefore, the CCVC is the most visited and studied geosite to date.
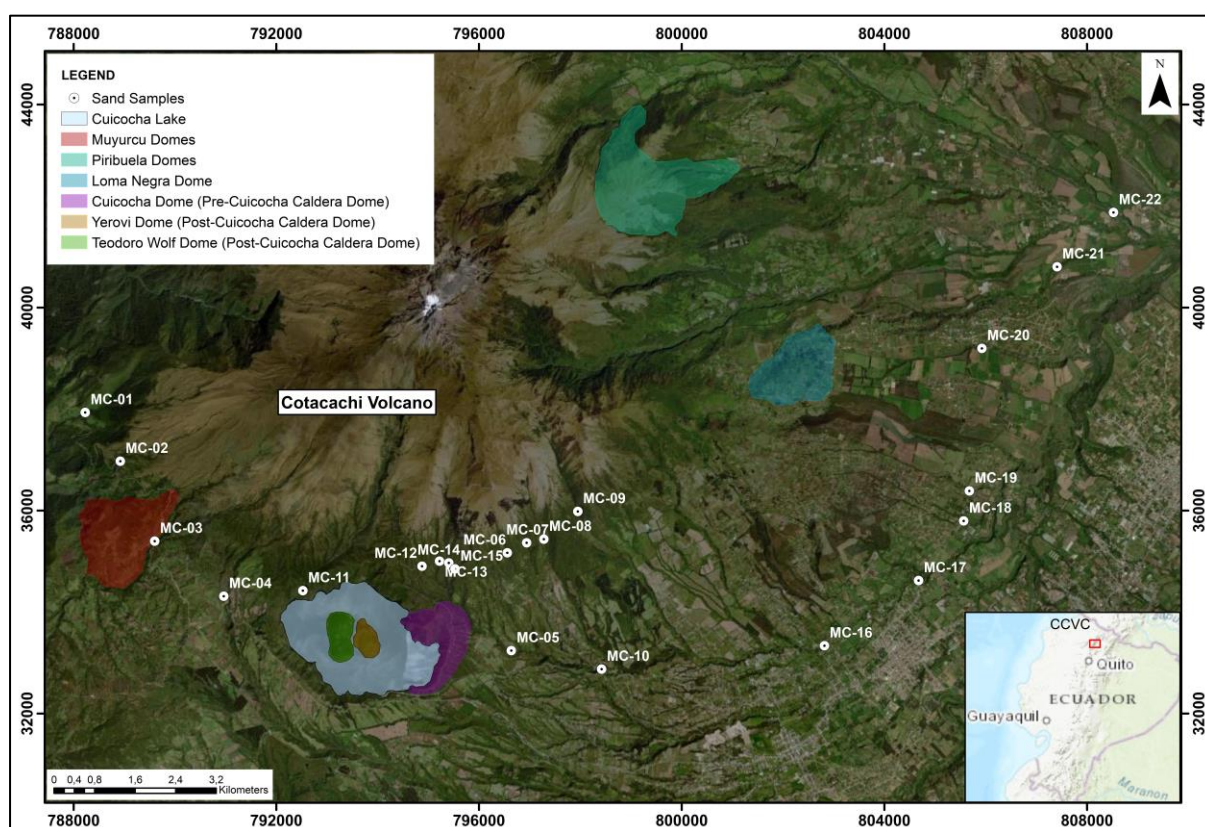
Figure 1. Cotacachi-Cuicocha Volcanic Complex view from the Google Earth satellite image. The white dots on the map indicate sample collection location and the colored polygons the different domes that make up the volcanic complex. Based on García (2020), Almeida (2016) and Von Hillebrandt (1989).

CCVC has several investigations focused mainly on its central stratovolcano and the evolutionary history of the formation of the Cuicocha caldera. One of the first investigations was carried out in 1989 by Christa Glee Von Hillebrandt Mayo and is a master's thesis entitled

"Geo-volcanic Study of Cuicocha - Cotacachi Volcanic Complex and its Implications, Imbabura Province." Among other relevant works is the master's thesis elaborated by Abigail Pidgen in 2014 entitled "Cuicocha Volcano, Ecuador: Reconstruction of major explosive phases through investigation of associated pyroclastic deposits," as well as the ungraduated thesis on the petrographic and geochemical study of the Cotacachi volcano by Marcos Andres Almeida Vaca in 2016, author who together with other researchers recently published a scientific article entitled New geological and geochronological constraints on the evolution of the Cotacachi - Cuicocha volcanic complex (Ecuador). Sierra et al., 2021 and Patrón et al., 2008 also contributed to the investigation of this complex with two scientific papers related to the CO_2 emission from the Cuicocha caldera. These and other investigations show the great relevance of the CCVC.

Despite several relevant investigations on the CCVC, it is evident that there needs to be research on the characterization of the fluvial sands associated with this volcanic complex. These sands are particularly found in fluvial systems. In this case, in a radial fluvial system associated with the geoforms of this complex that supplies multiple hydrographic basins nearby. These, in turn, carry sand-sized particles that are both lithic and mineral fragments associated with the pyroclastic deposits of the complex and that come from the higher areas of the complex, so they have not undergone significant transport. Thus, the particles are not contributed directly by volcanic body, the particles of pyroclastic deposits are eroded by the extensive fluvial systems in which heavy minerals (HM) are usually prospected.

Certain heavy minerals are crucial for global technological advancement (Ochoa, 2022). However, there are many untapped sources of minerals, such as mineral sands. In most cases, when we refer to "mineral sands," we imply concentrations of heavy minerals in an alluvial environment, like an ancient beach or a river system (Jones, 2009). Ilmenite, rutile, zircons, magnetite, and monazite are the main types of these heavy minerals and are frequently a source of rare earth elements (Ochoa, 2022). The periodic table group of seventeen chemical elements known as rare-earth elements (REEs) consists of the elements in the lanthanide series (La, Ce, Pr, Nd, Pm, Sm, Eu, Gd, Tb, Dy, Ho, Er, Tm, Yb, and Lu) as well as Sc and Y (Balaram, 2019). The rare earth elements can be found in several types of mineral deposits, although these deposits are very sparse (De la Hoz, 2012); particularly, these minerals are present in negligibly small quantities. The igneous, sedimentary, and metamorphic rocks that contain rare earth elements have undergone igneous, hydrothermal, or secondary sedimentary processes to enrich

them with these elements. (Montero, 2012, as cited in Pérez, 2019). In igneous rocks, the rare earth elements have primarily been found in carbonated, alkaline, peralkaline, and pegmatite rocks, primarily in countries like China, Australia, Russia, the European Union, Canada, and Brazil, among others, and have played a significant role in the rising industrial demand since the 1970s (Márquez & Jiménez, 2017). In contrast, the only activity in the study area that involves using geological materials is the extraction of stone quarries, which have aggregates of building stone, gabion stone, and rock boulders.

The geology of Ecuador is highly diverse (Carrión et al., 2022), In addition to heavy minerals in fluvial courses in Esmeralda province (Mendoza et al., 2023), there are many locations where river sands might accumulate and potentially contain valuable minerals that have not yet been identified. As a result, this work could be utilized in several locations to find and utilize these natural riches since these natural resources are currently crucial in research and industrial and economic development. Therefore, this thesis aims to provide relevant information on the sands associated with the CCVC, including their morphometric analysis, mineralogical association, industrially valuable minerals, REEs, and possible uses and applications. Thus, this work integrates granulometric analysis, stereomicroscopic observations, magnetic separation, and qualitative and quantitative analyses (X-ray diffraction, Raman spectroscopy, and X-ray photoelectron spectroscopy) of the minerals present in the sands associated with the CCVC.

1.1   Problem Statement

The CCVC is of particular interest due to its eruptive history that has resulted in the formation of different geomorphologies and the expulsion and modification of some materials, such as rocks and sands. These sands may contain some minerals and REEs, probably minerals and elements of industrial and economic interest. However, although there are several studies related to the geology, geomorphology, and formation of the volcanic complex, there have yet to be studies focused on the characterization of these minerals and their possible applications. Therefore, researching the subject will complement the existing information and increase our knowledge. Important information that will help to take advantage of these mineral resources.

1.2   General Objective

- Characterization of the sands associated with the Cotacachi–Cuicocha Volcanic Complex.

1.3   Specific objectives

- Perform a morphometric analysis of lithic fragments and sand-sized particles associated with the Cotacachi-Cuicocha Volcanic Complex.

- Determine the mineralogical association of the sands by analytical techniques, granulometric determination methods, stereomicroscopic observation, X-ray diffraction, and Raman spectroscopy.

- Identifying industrially valuable minerals and determining the fraction where the highest concentration of these minerals is found.

- Propose possible uses for the minerals more representatives identified in the fluvial sand associated with the CCVC.

- Determine the existence of rare earth elements by X-ray photoelectron spectroscopy.

CHAPTER 2: GEOLOGICAL FRAMEWORK

This chapter addresses the most relevant aspects of the geodynamic environment of Ecuador and the Cotacachi-Cuicocha Volcanic Complex, including a brief description of each geoform that makes up the complex.

2.1   Ecuadorian geodynamic environment

The vast Ecuadorian geodynamic environment has given rise to significant geological events that have profoundly imprinted the Ecuadorian geologic record (Villagómez, 2003). The convergence of tectonic plates is one of these episodes and is considered one of the most critical in Ecuador. This event is the leading cause of volcanism, a deformation on South America's western margin, and the formation of an orogenic system in Ecuador (Andean Orogeny) (Villagómez, 2003). This orogenic system crosses from north to south through Ecuadorian territory. Thus, the convergence of tectonic plates and other events have also led to the formation of two significant mountain ranges with approximate N-S direction, the Western Cordillera and Eastern Cordillera (Cordillera Real) (Villagómez, 2003). Additionally, the Inter-Andean Valley is located in the center of these two mountain ranges and has the same direction. Most of the volcanoes with summits higher than 6000 meters are formed on these two cordilleras, which have an average elevation of 3500–4000 meters above sea level (Hall et al., 2008).

Some authors call Ecuador a small Andean country with a striking volcanic arc home to numerous active and potentially active volcanoes (Hall et al., 2008). The Ecuadorian Andes are a result of the subduction of the Nazca plate beneath the South American plate (Barragan et al., 1998). In Ecuador, it is approximately a 650 km long and 150 km wide mountain range (Hall et al., 2008). At least 84 Quaternary volcanoes have been cataloged by Bernard & Andrade (2011) along the Ecuadorian Andes (Figure 2). Based on their most recent eruption, they have been categorized as follows: 58 extinct, 17 potentially active, 5 active, and 3 volcanoes erupted between 2011 and 2015 (Almeida, 2016). In addition, 11 of these volcanoes are located in the Imbabura Geopark (Jácome et al., 2020). Therefore, Imbabura province is characterized by its impressive elevations and volcanic history; the Cotacachi-Cuicocha Volcanic Complex is a clear example.
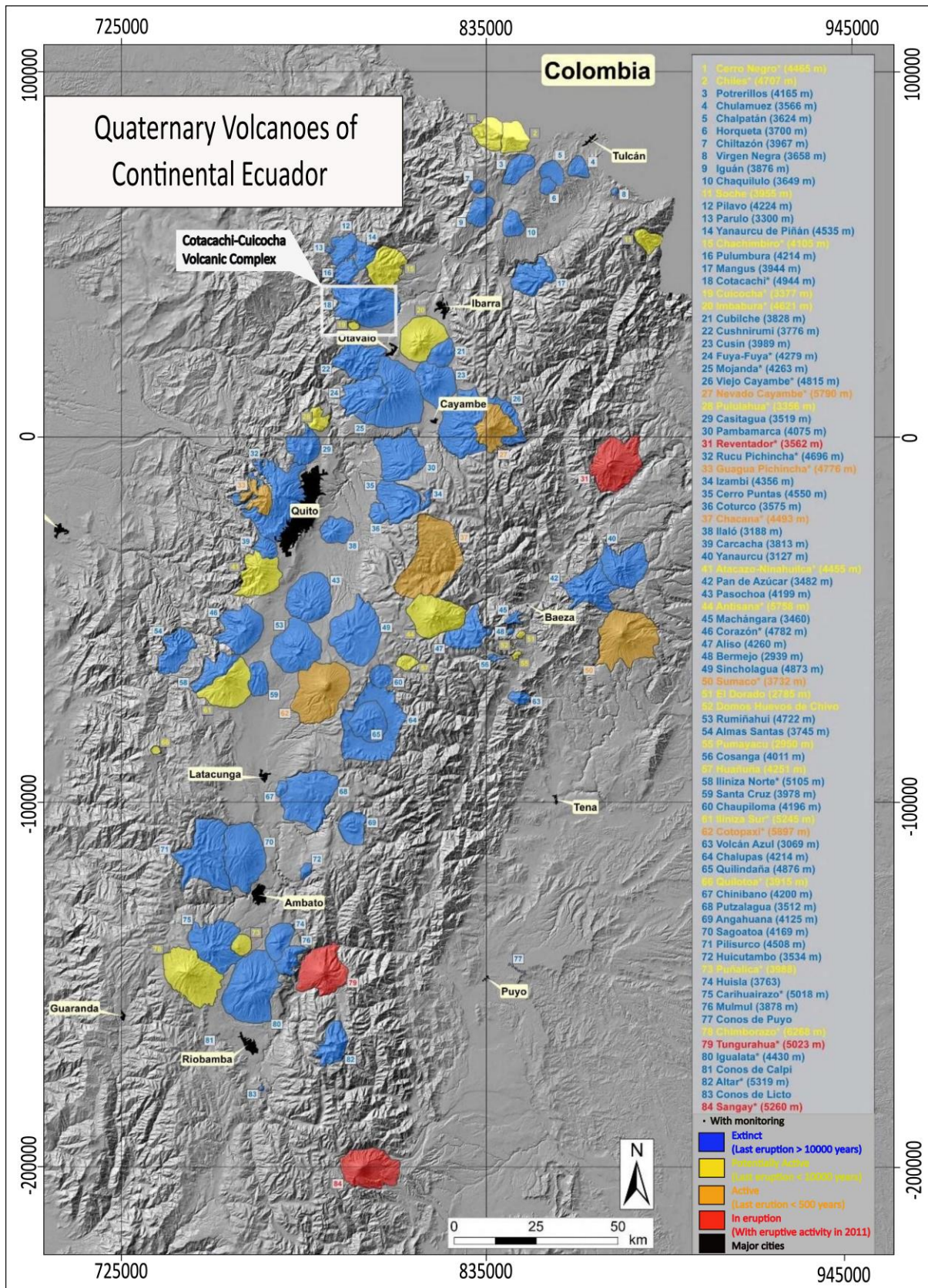
Figure 2. *Extinct, Potentially Active, Active and Erupted Quaternary Volcanoes of Continental Ecuador. Modified from Bernard & Andrade, 2011.*

2.2   Cotacachi-Cuicocha Volcanic Complex (CCVC)

The CCVC (Figure 1,2,3), located at Imbabura Geopark, forms part of the Western Cordillera and borders the inter-Andean valley of the Ecuadorian. It has a surface area of around 260 km^2 (Sierra et al., 2021). Save for its central volcano, the CCVC is considered potentially active (Almeida, 2016). It comprises several emission centers, ranging in age from older to younger, including Cotacachi, Muyurcu, Loma Negra, Peribuela, and Cuicocha (Von Hillebrandt, 1989). Further, this complex is associated with developing the Cuicocha crater lake with the islets Yerovi and Teodoro Wolf inside.

There are several different geological bodies inside the CCVC, including dacite and andesite rocks, dacitic tuff, alluvial deposits, avalanche deposits, and next to the Muyurcu domes part of the Rio Cala Unit (Figure 3). Additionally, there are many different types of volcanic deposits associated with the complex, including massive pyroclastic flows, surges, fall deposits, lava flows, lava collapse flows, and lahars, which are interspersed with primary volcanic deposits and reworked volcanic material from other volcanoes like Imbabura, Chachimbiro and Mojanda (Von Hillebrandt, 1989). Therefore, the CCVC has been involved in several eruptive events that have deposed different materials throughout the complex. Pyroclastic flows that reached Otavalo and Cotacachi and deposits of "block and ash" debris from the development and collapse of the domes are among the event's distinctive deposits (Vallejo, 2011). The volcanic complex eruptive style may be determined by the compositional diversity of the magma emitted by the eruptive centers of the domes (Augusto, 2019). While Loma Negra, Peribuela, and particularly Cuicocha eruptions were explosive and produced pyroclastic flows and fall, Cotacachi and Muyurcu eruptions were primarily passive with the emission of lava flows and the formation of domes (Von Hillebrandt, 1989). Therefore, there are variations of the material in the Cotacachi volcano and the domes that make up the CCVC (Figure 3). The Cotacachi and Muyurcu consist mainly of andesitic rocks, Loma Negra and Peribuela are comprised of andesitic/dacitic, and Cuicocha have dacitic rock compositions (Von Hillebrandt, 1989), like the Yerovi and Wolf domes.
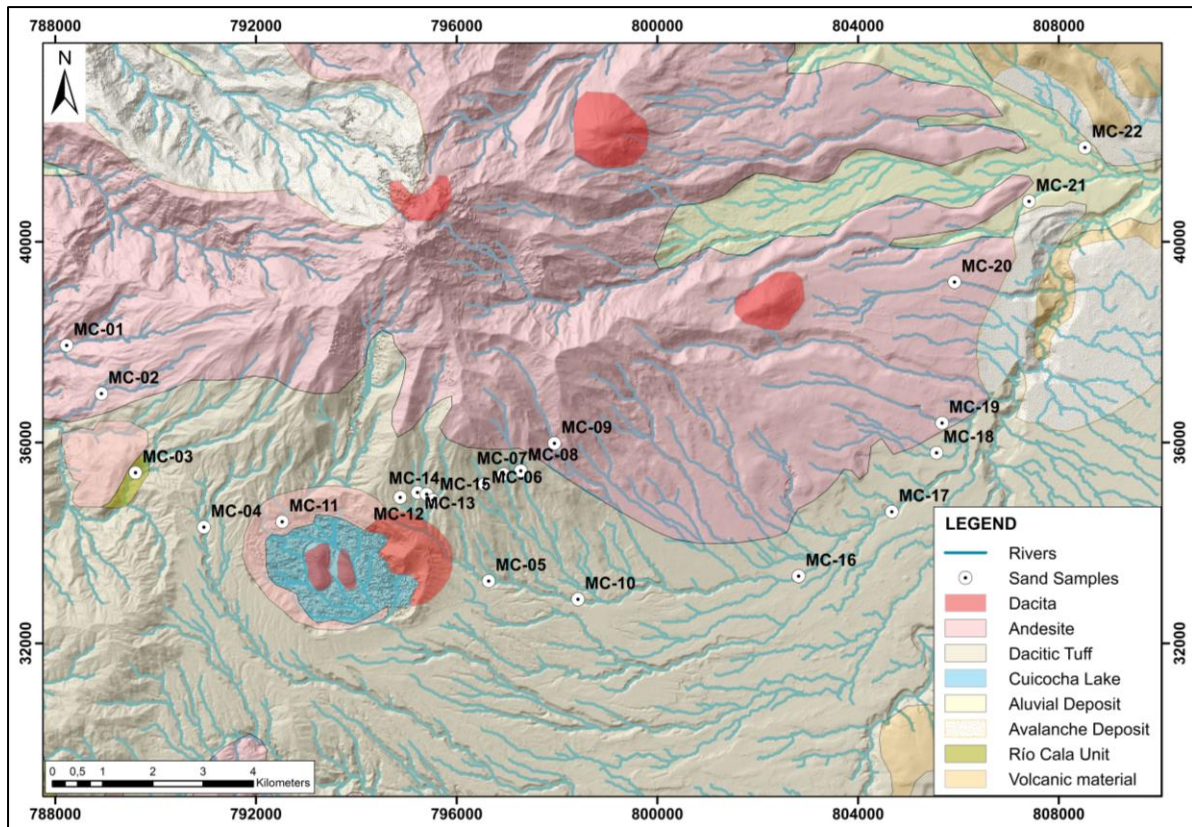
Figure 3. *Geological Map of Cotacachi-Cuicocha Volcanic Complex. The blue lines on the map indicate the tributaries of water, the white dots indicate sample collection location and the colored polygons the different lithologies. Modified from Boland et al., 2000.*

2.3   Cotacachi Volcano

This volcano is the oldest central eruptive edifice of the CCVC (Figure 1,2,3), and its volcanic activity dates back to the Pleistocene (Von Hillebrandt, 1989). Thus, it is considered an extinct or dormant volcano (Almeida, 2016). Cotacachi volcano of basaltic-andesitic composition (Augusto, 2019) was formed at the base igneous basement of Western Cordillera, located at 4944 m.a.s.l. (Jácome et al., 2020). The volcano is around 11 km^2 in length from east to west and 13 km from north to south (Von Hillebrandt, 1989), and it has an andesitic lava flow pseudo-pyramidal erosional structure (Jácome et al., 2020). It is very eroded due to the severe glaciation it has experienced (Von Hillebrandt, 1989). It underwent two massive avalanches of debris during its history, forming the first volcanic edifice, the first structure topped by lava flow intercalations between 162 and 108 million years old (Jácome et al., 2020). The second building is currently constructed on top of it and resembles a "pyramid" in shape (Almeida, 2016).

2.4   Muyurcu Domes

Muyurcu domes (Figures 1,4) are found on the Cotacachi volcano's southwest flank, are a collection of several domes with a maximum height of 3502 m.a.s.l. and cover an area of around 2.35 km^2 (Almeida, 2016). The domes appear to have developed after the Cotacachi volcano because they have less erosion than the volcano (Von Hillebrandt, 1989). The grey vesiculated and porphyritic andesite is the primary material that makes up the dome (García, 2020).
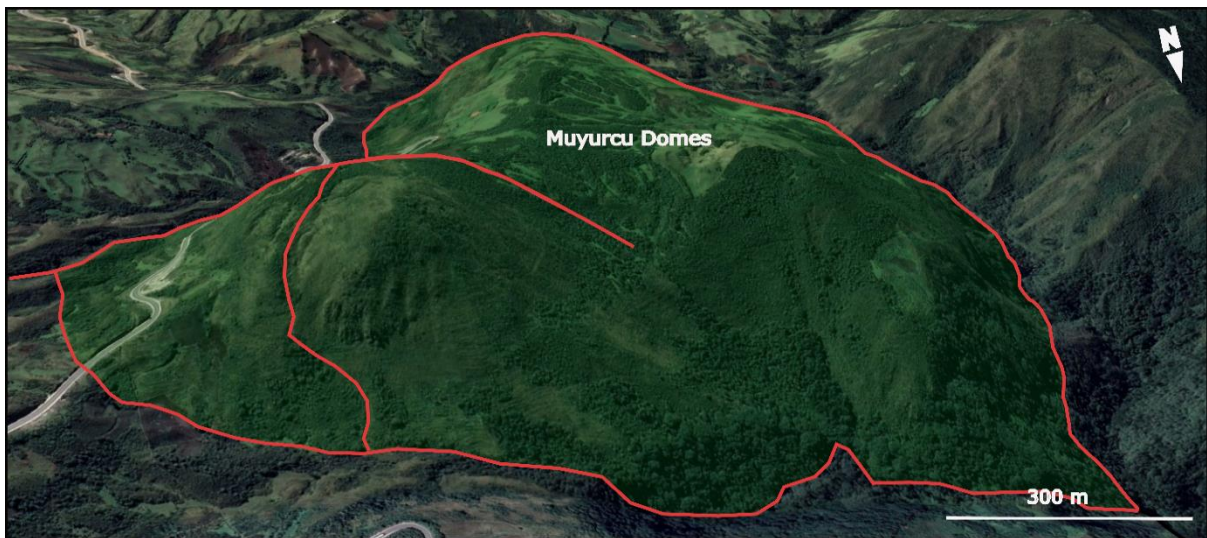
Figure 4. Satellite Google Earth imagen of Muyurcu Domes. The red lines indicate the approximate outline of the domes.

2.5   Loma Negra dome

Loma Negra dome (Figure 1,5) is located on the southeast flank of the Cotacachi volcano. The dome is at an elevation of 3055 m.a.s.l. and covers an area of around 1.7 km^2 (Almeida, 2016), and is mainly made up of hornblende andesite rocks (Von Hillebrandt, 1989).
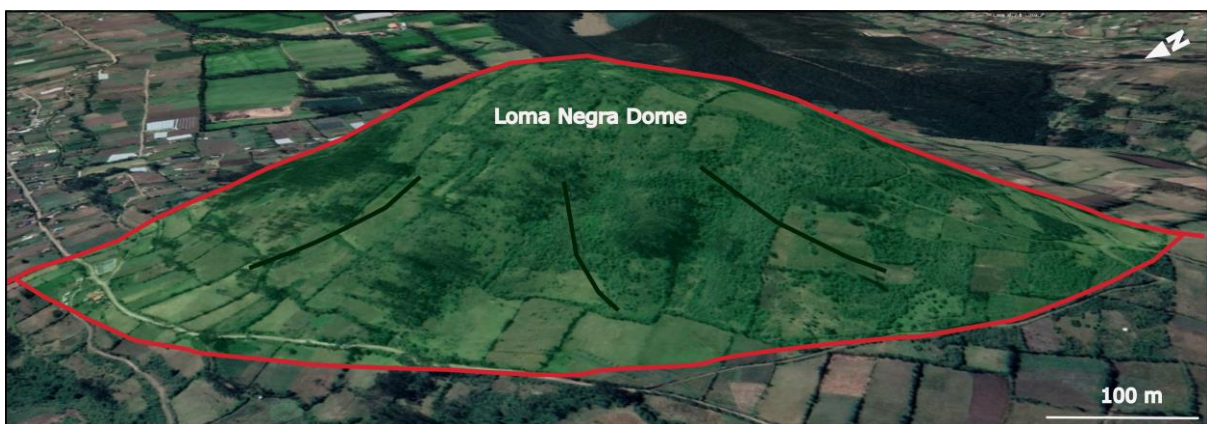
Figure 5. Panoramic view from Google Earth of the Loma Negra dome. The red line indicates approximate outline of the dome.

2.6   Peribuela Domes

Peribuela domes (Figures 1,6) are located on the volcano's northern flank; they are oriented N-S, cover an area of around 3.8 km², and reach a maximum height of 3871 m.a.s.l. (Almeida, 2016). The Oriental portion of this dome has a scar that caused a significant landslide (Von Hillebrandt, 1989). Plagioclase, amphibole, and trace amounts of pyroxene and biotite are the main phenocrysts found in the dacitic lavas of these domes (Almeida, 2016).
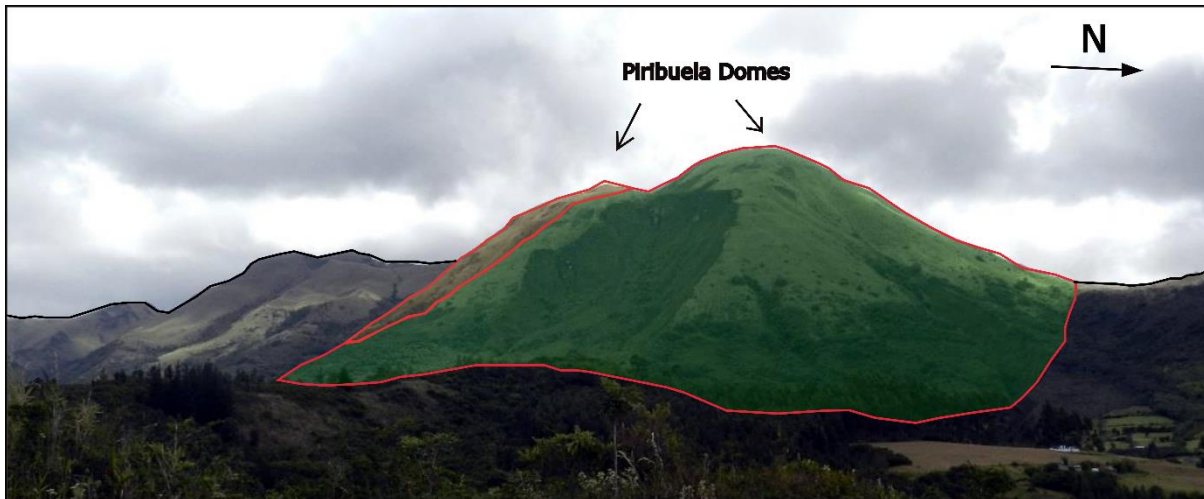
Figure 6. Imagen of Peribuela Domes. The red line indicates approximate outline of the domes. Modified from Almeida 2016.

2.7   Remanent Cuicocha Dome

The remanent Cuicocha dome (Figures 1,7) is located in the southern part of the flank now extinct Cotacachi stratovolcano (Padrón et al., 2008), has a height of 3377 m.a.s.l. and constitutes a sizable portion of the eastern lake border (Almeida, 2016). The presence of slope deposits near the dome leads experts to believe that the current structure is simply a fragment of a dome with a diameter of up to 1.5 km (Von Hillebrandt, 1989). It is the result of several events, most notably volcanic eruptions. This partial dome destruction occurred approximately 3100 years ago while the caldera was forming (Von Hillebrandt, 1989).

Figure 7. *Satellite Google Earth imagen of Cuicocha Dome. The red line indicates outline of the dome.*

2.8 Cuicocha Caldera

Caldera Cuicocha (Figures 1,3,8) is located on the SSW of Cotacachi volcano and is considered active. The caldera is roughly 3.2 km long from east to west and 2.2 km wide from north to south, and it has an atypical oval shape (Von Hillebrandt, 1989). Numerous eruptive episodes, mainly the release and storage of pyroclastic material, led to the caldera formation. The water from the Pleistocene Cotacachi volcano deglaciation, precipitation, and hydrothermal water have combined to create a lake with a maximum depth of 148 meters, a lake capacity of 0.28 km^3, and a surface altitude of 3072 m.a.s.l. (Padrón et al., 2008). In addition, two port-caldera domes have formed within the lake due to eruptive episodes, Yerovi and Wolf. These two domes, often known as islets, are in the Cuicocha lake center. There is a clear difference in size between the two domes. Yerovi has an approximate area of 0.26 km^2, and an altitude of 3062 m.a.s.l. while Wolf has an approximate area of 0.44 km^2, and an altitude of 3247 m.a.s.l. in the northern part of the dome and 3202 m.a.s.l. in the southern part (García, 2020).
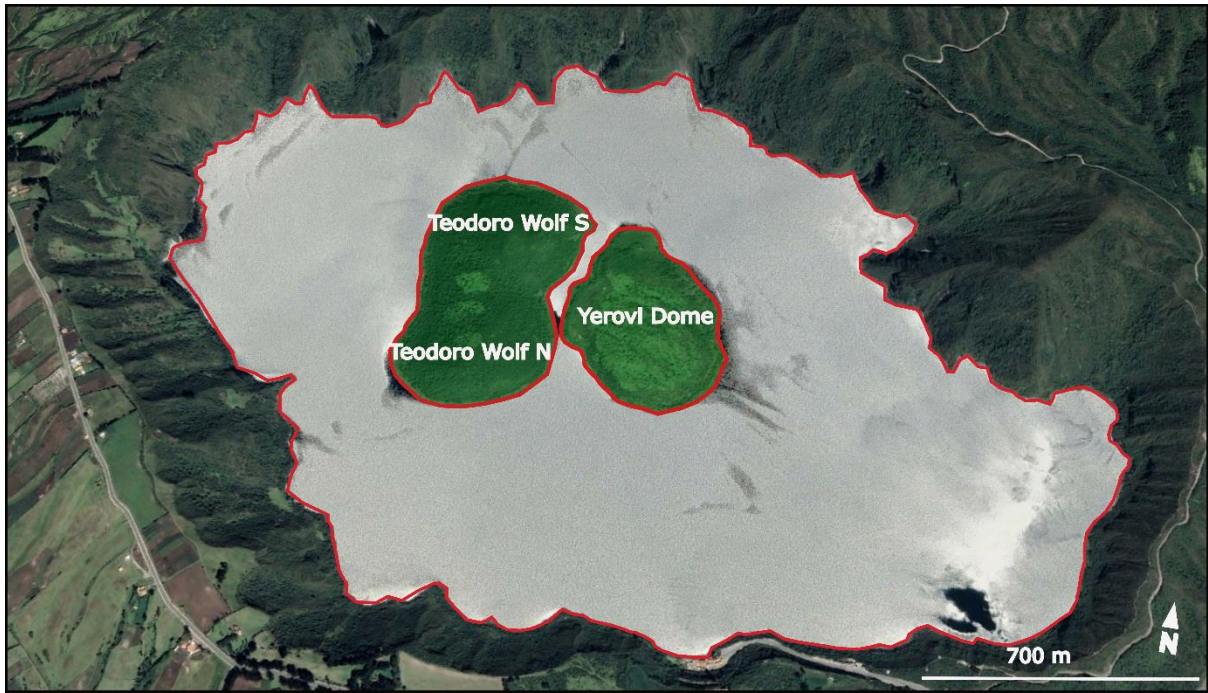
Figure 8. *Satellite Google Earth imagen of Teodoro Wolf and Yerovi domes. The imagen shows in red the outline of the islets and the Cuicocha lake.*

CHAPTER 3: METHODOLOGY
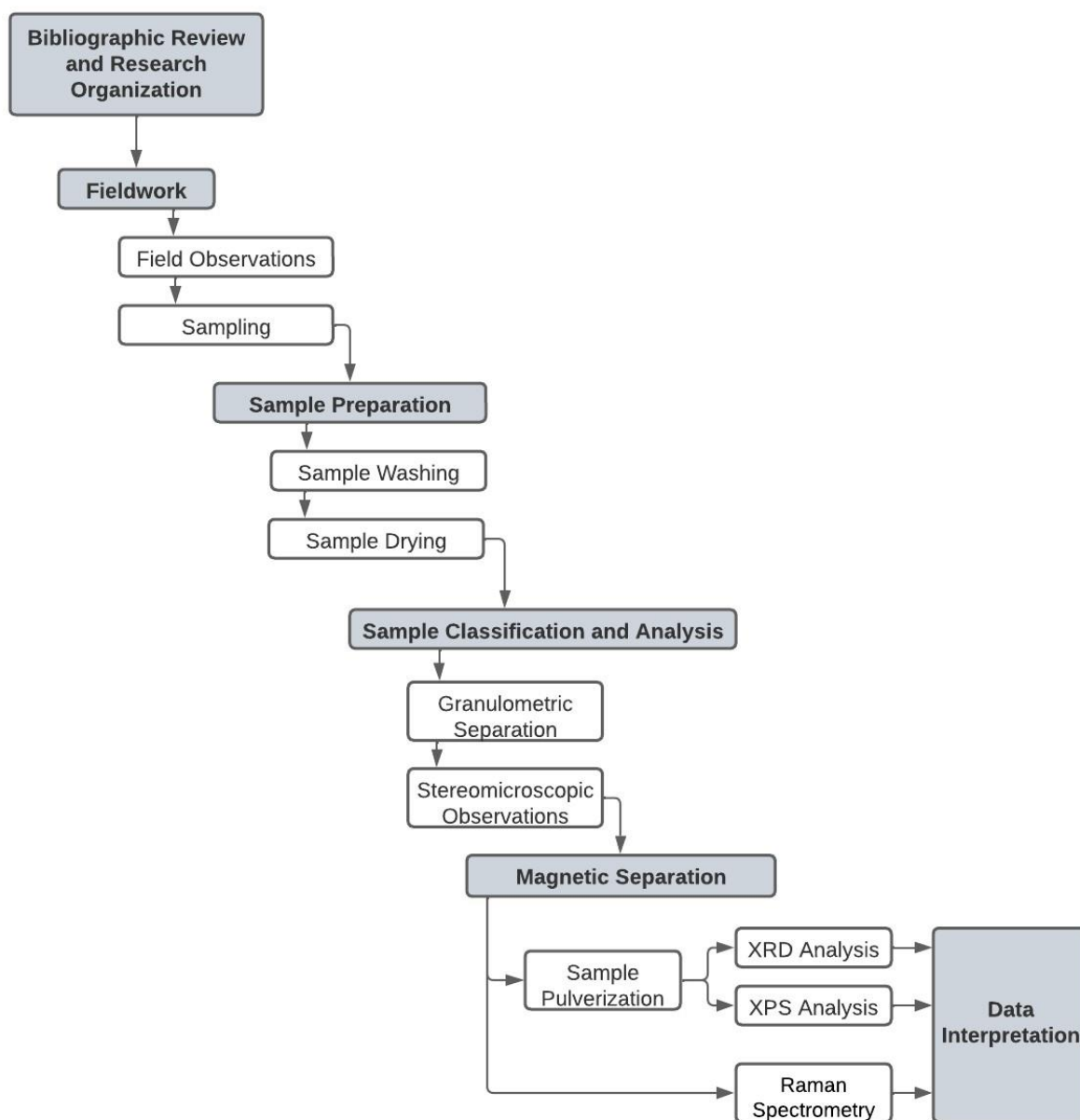
Figure 9. Diagram of the methodology used to achieve the research objectives.

3.1   Sampling

Sampling was organized using an earlier design and the planning of potential locations for sample collecting. A map was created of the area with the locations of the various rivers, and it was suggested that sand samples be taken at each of the 30 potential sampling locations, numbered from west to east.

Several field trips were necessary for the collection of the samples. Nevertheless, only 22 samples of 30 previously planned could be collected due to restricted tributary access (Figure 10). They were collected from the river channels in the flat areas where a large amount of sand accumulated, approximately 200 degrees southeast, around the Cotacachi volcano. However, taking samples from the northwestern part of the volcano was impossible due to difficult access. The sampling sites were determined considering the first and second-order causes, which subsequently allowed us to relate the origin of the sediments with the geological formations that outcrop in the study area.
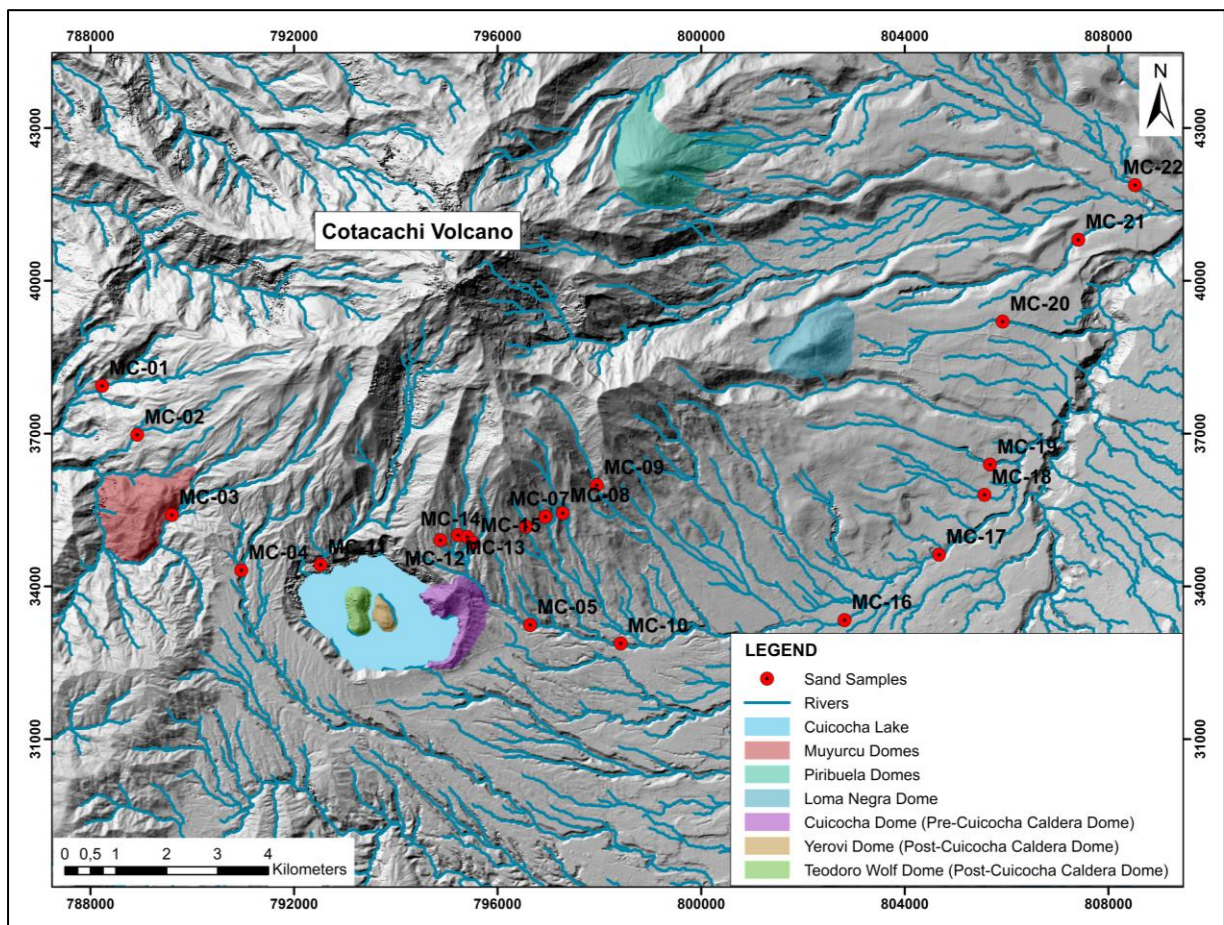
Figure 10. *Sampling points. It shows the 22 exact points where the samples were collected.*

The samples were coded with the initials MC; these initials refer to Cuicocha samples in Spanish (Muestras de Cuicocha) plus a number representing the order in which they were collected (Table 1).

Table 1. List of coordinates of samples collected. The left side shows the code designated to each sample and the right side the coordinates in degrees minutes seconds in the names of each sample. See location in figure 1, 3, 10.

Samples Name	UTM Coordinates (17N)	
	East	Norte
MC-01	788230	37935
MC-02	788922	36974
MC-03	789602	35399
MC-04	790965	34314
MC-05	796640	33242
MC-06	796560	35169
MC-07	796941	35366
MC-08	797281	35437
MC-09	797952	35984
MC-10	798421	32877
MC-11	792525	34423
MC-12	794877	34905
MC-13	795222	35005
MC-14	795405	34970
MC-15	795528	34851
MC-16	802819	33338
MC-17	804676	34622
MC-18	805567	35796
MC-19	805678	36389
MC-20	805926	39197
MC-21	807410	40805
MC-22	808524	41876

3.2   Sample washing

The preparation of samples begins with a purification of the sands. It is necessary to depurate sand since some samples exhibit a variety of impurities and are, therefore, unsuitable for its preparation (Chuquirima & Cortez, 2014). Therefore, fine sediments were sampled by removing impurities and rock clasts larger than 3 mm with the help of a sieve (Figure 11A). The sample that passes through the sieve is collected in a container, in this case, a 5-liter bucket. Then, a first washing is performed to eliminate clay material (Figure 11B). After that, a second washing removes unnecessary surplus material (Figure 11C). Finally, between 2000 to 2500 g of samples were placed in previously labeled zip lock bags (Figure 11D, E). This process was carried out for all samples; in the case where the river channels had no water, the same process was carried out in a laboratory.

Figure 11. Sample washing and storage. A) Sample sieving. B) Removal of clays with a first wash. C) Second wash. D, E) Sample storage and labeling.

3.3 Sample drying

In order to obtain a dry sediment, moisture must be removed through the drying process, which typically entails separating a liquid from a solid by evaporation (Gutierrez & Rondon, 2018). This will allow the sample not to agglomerate and is easier to handle, besides being a necessary process for subsequent processes.

The sample drying process starts with the distribution of the sample in a container and then applying the quartering method so that the sample components are well distributed. The quartering method consists of distributing the sample on a surface, dividing it into four parts, and taking two (Figure 12A). The two parts are adjacent and placed in a beaker for later weighing (Figure 12B). This procedure is repeated for all samples. Once the samples are weighed (700 to 810 g) and labeled, they are placed in the laboratory stove oven provided by chemical laboratory at Yachay Tech University (Figure 12C). The samples are placed in the oven at a temperature of 100°C, 8 hours per day for five days. The weights

are recorded to verify that the samples are dry when each samples humidity percentage is minimal. It can be calculated by applying the formula:

$$H\% = \frac{W_W - W_D}{W_W} \: x \: 100 \qquad (1)$$

Where:

$H\%$ = Percentage of humidity

W_W = Weight of wet sample

W_D = Weight of dry sample

Figure 12. Process of sample drying. A) Applied to quartering method. B) Sample weighing. C) Laboratory stove

3.4 Granulometric Separation

The distribution of particle sizes at which rocks, minerals, or other materials are found can be determined using granulometric analysis; this information helps recognize, classify, isolate, concentrate, and recover the desired elements (Kerguelen, 2016), as in the case of this study.

The granulometric separation was performed at 500 g of each sample. This procedure was carried out in the vibratory sieve shaker provided by the laboratory of sample preparation and crushing of the School of Earth Sciences, Energy and Environment at Yachay Tech. Table 2 shows the aperture in millimeters and the number of meshes used for this analysis.

Table 2. *The particle size analysis used meshes and their respective apertures in millimeters.*

Mesh	Aperture diameter (mm)
10	2
18	1
35	0.5
60	0.25
120	0.125
230	0.063
<230	Rest

Initially, the 500 g of sample was placed on the sieves previously ordered from the smallest to the largest, covered, and placed in the vibrating sieve shaker. Each sample was sieved for 40 minutes (Figure 13A). The different fractions are placed in zip lock bags and labeled again with the name of the sample plus the corresponding mesh number from which the sample was collected (Figure 13B) and weighing (Figure 13C).
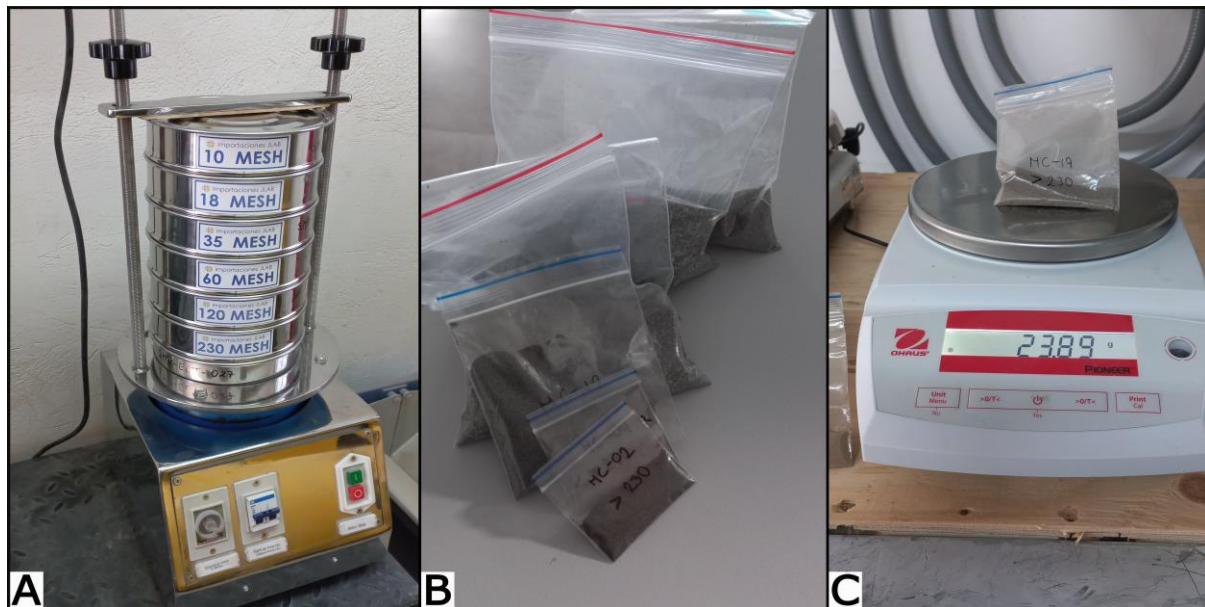
Figure 13. *Granulometric separation. A) Granulometric separation of 500 g of sample in the vibrating sieve shaker for 40 minutes. B) Storage and labeling of the fractions collected in the different sieves. C) Weighing of the different fractions obtained.*

The data was recorded to transform into percentages with a formula 2. It is necessary to determine the three most representative fractions and take them to stereomicroscopic observations.

$$M\% = \frac{W_p * 100}{W_t} \tag{2}$$

Where:

$M\%$ = Percentage of different portions obtained of each sample.

W_p = Weight different portions obtained.

W_t = Total sample weights before granulometric separation.

3.5 Stereomicroscopic observations

In this study, the stereomicroscopic observation allows differentiating minerals concerning their physical characteristics, among the most relevant: shape, color, and luster. Seven samples, equivalent to 33.3% of the total samples, were chosen for this analysis, taking the three most representative fractions from the granulometric analysis. The seven samples were selected at random, trying to ensure that they were distributed along the entire length of the CCVC. Once chosen, place a fraction of the sample on a slide for a thorough analysis.

Each fraction is analyzed under the Olympus AXZ16 stereomicroscope provided by the nanotechnology laboratory of Yachay Tech University (Figure 14A). A reconnaissance of minerals or lithics is performed. For this purpose, a photographic record of the 35, 60, and 120 mesh fractions is created with a focus of 1, 2, and 3.2 respectively. In order to obtain a representative count of the minerals present in each sample and a first mineralogical characterization, a total of 10 fields were observed, with a total count of 300 points for each fraction. The photographs of each field were analyzed using OLYMPUS Stream Essentials software (Figure 14B). Each field was divided into four parts, and the minerals from two opposite sections were counted (Figure 14C). With this procedure, it was possible to determine the fraction with the highest abundance of minerals of possible industrial interest, which would be used for analysis by Raman spectroscopy, XRD, and XPS analysis.
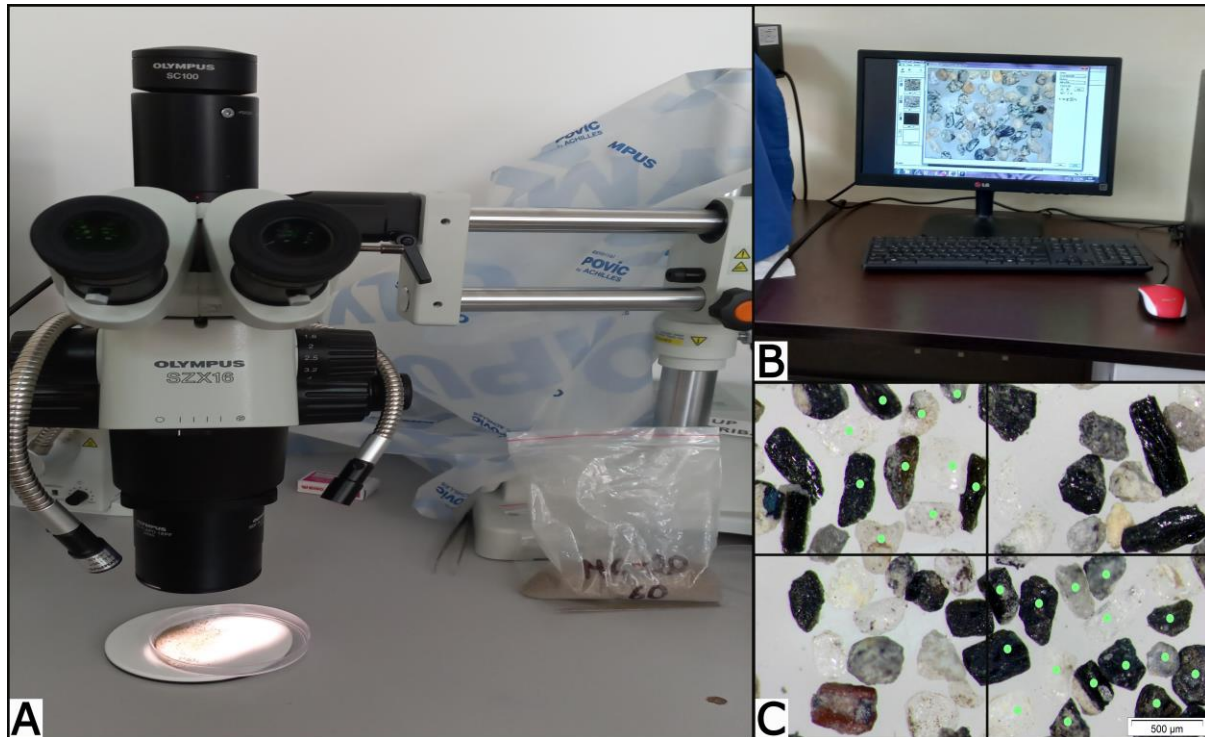
Figure 14. A) Olympus AXZ16 stereomicroscope. B) Photographs uploaded to the OLYMPUS Stream Essentials software. C) Grain counting and recognition.

3.6   Magnetic separation and sample pulverization

Magnetic separation is based on grouping or separating minerals according to their magnetic susceptibility when exposed to a uniform magnetic field and a constant velocity (Londoño et al., 2010). It is commonly used in geology to group minerals with high iron content. Thus, this technique is performed to identify or to determine relative proportions amongst minerals based on the weight of the magnetically separated fraction (Londoño et al., 2010).

Magnetic separation is performed on the fraction collected in the 120 mesh of the samples previously analyzed in the stereomicroscope to separate the minerals according to their degree of magnetism. A first manual separation is performed using a neodymium magnet (Figure 15A), where a large fraction of magnetic material is obtained. The second magnetic separation is performed with the Frantz, Magnetic Barrier Laboratory Separator (Model LB-1), provided by the laboratory of thin sections, magnetic separator, and sample crusher of the School of Earth Sciences, Energy and Environment at Yachay Tech (Figure 15B). The Frantz was adjusted to 30 degrees of inclination, and varying the frequency to 0.2 amperes to separate the magnetic minerals, 0.35 amperes for the low-magnetic minerals, and having as a remainder of the process the non-magnetic fraction. The fractions are labeled again with the name of the

sample plus the corresponding mesh number from which the sample was collected and the letters M, L, or N, referring to magnetic, low-magnetic, and non-magnetic (Figure 15C). The fractions obtained are quantified to obtain the percentage of sand.

Figure 15. *Magnetic separation. A) Manual separation used to neodymium magnetic. B) Frantz magnetic separator. C) Fractions separation.*

Part of the three fractions obtained from the magnetic separation of the seven samples is used for analysis from Raman Spectroscopy, and the other part is pulverized for subsequent XRD and XPS analysis. The pulverization procedure is performed manually using an agate pestle and mortar (Figure 16A). The pulverized samples are sieved in a 230 mesh (Figure 16B) and pulverized again to make them as fine as possible until a talc-like texture is obtained. The resulting samples are properly stored and labeled with the same name (Figure 16C).

Figure 16. Sample pulverization. A) Pulverized hand. B) Sieved Samples. C) Ready samples.

3.7   X-Ray Diffraction (XRD)

A high-tech, non-destructive method for analyzing a wide variety of materials is X-Ray diffraction (Cerquera et al., 2017). It is a flexible analytical technique for identifying and quantifying the presence of crystalline phases in powdered and bulk samples (König & Verryn, 2021). In geology, crystalline phases help us determine the type of mineral present in a sample. The crystalline phases within a sample can be recognized by comparing the diffraction data to

a database of Known materials (König & Verryn, 2021). Since each mineral type is distinguished by a specific crystal structure, resulting in a distinctive X-ray diffraction pattern (Bunaciu et al., 2015). However, there are several limitations to this analysis. This technique commonly helps us to recognize the predominant crystalline phases in the samples since a minority phase must be present in the sample whose relative concentration must be greater than 5%. (Alba & Sato, 2008, as cited in Galán et al., 2009).

The basis for the X-Ray Diffraction is the optical interferences that result from monochromatic radiation passing through a slit with a length equivalent to the wavelength of the radiation (Cerquera et al., 2017). When radiation strikes a solid, periodically spaced atoms coherently scatter the radiation, creating scattered beams that generate spot patterns in single crystalline samples and ring patterns in polycrystalline materials (Khan et al., 2020). As a result, the X-ray diffraction pattern represents a material's fingerprint of periodic atomic groupings (Bunaciu et al., 2015). However, a particular process must be followed to discover this pattern.

The XRD analysis was performed in the materials characterization laboratory of the School of Chemical Sciences and Engineering at Yachay Tech University. They were analyzed 21 fractions corresponding to the magnetic separation on the seven samples previously used in the stereoscopy analysis. XRD analysis starts by placing the well-powdered samples in the sample holders; placing the samples as compact and flat as possible is necessary. The sample is placed with the help of a spatula, flattened with an object cover, and a brush is used to remove the excess material (Figure 17A).

The analysis was performed with an X-ray diffractometer for polycrystalline samples (Figure 17B), equipped with a 600W X-ray tube, Bragg-Brentano goniometer with 8-position autosampler (Figure 17C), D/teX Ultra detector, SmartLab Studio II software. Under the following measurement conditions: X-ray generator operated at 40 kV and 15 mA, CuK(alpha) radiation source (sealed tube), a Theta/2Theta scanning axis, 0.0025° pitch width, 5-70° scanning range in 2Theta, and D/tex Ultra2 detector in 1D scanning mode were used for data acquisition.

Once the corresponding data have been obtained, the crystalline phases are identified. It was identified through a series of steps and with the help of the Match! software. This software made it possible to compare the results obtained with a database of Crystallography Open Database Called COD-Inorg 2022.
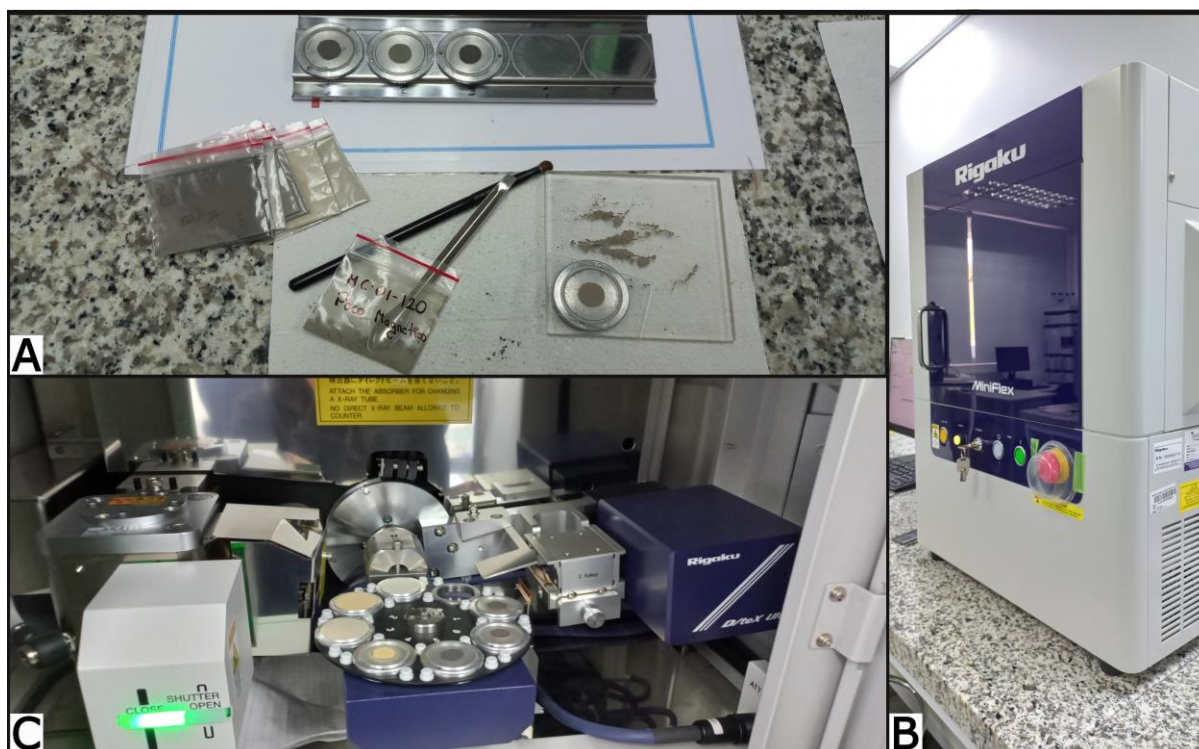
Figure 17. DRX analysis. A) Materials to preparation of samples. B) X-Ray Diffraction (DRX). C) Samples ready placed inside the X-ray diffractometer.

3.8   Raman Spectroscopy analysis

Raman spectroscopy is a non-destructive analytical technique. It is a method that reveals specific information about materials, whether organic or inorganic, and being a high-resolution photonic technique may reveal chemical and structural details about it (Galán et al., 2009). It has a significant effect on the investigation of geological materials. It is mainly used to identify minerals, inclusions and to examine the crystalline phases (Galán et al., 2009).

Raman spectroscopy involves the interaction of the sample with monochromatic radiation (Caisachana, 2021), and the analysis of this radiation or light reflected by the material is through the use of a standard optical microscope connected to a Raman spectrometer (Galán et al., 2009). The reflected light comprises photons that may be absorbed or dispersed, or they may not interact with the material and pass right through it when light interacts with matter (Smith & Dent, 2019). The dispersed frequencies can be analyzed to learn more about the material's chemical makeup, condition, and other aspects (Galán et al., 2009), essential factors for the recognition of the different minerals present in the samples of this research.

The analysis of the minerals presents in the different samples of this research using a LabRam HR Evolution microscope was carried out in the laboratory of the School of Physics at Yachay Tech University (Figure 18A). This technological tool provides three lasers (532, 638, 785 nm); in this study, the 785 nm He-Ne laser and a 50x50 magnification objective were used. An accumulation of 7 spectra was set up, and the bean aperture was maintained open for 7 seconds.

The minerals of Interest are chosen and glued to the slide (Figure 18B) for their respective analysis and obtaining characteristic spectra. Using the software CrystalSleuth, the spectra obtained were compared with a RRUFF database which contains various Raman spectra of different minerals. Thus, it is possible to determine the corresponding minerals according to the similarity percentage and the wave number range in which the spectrum is found.
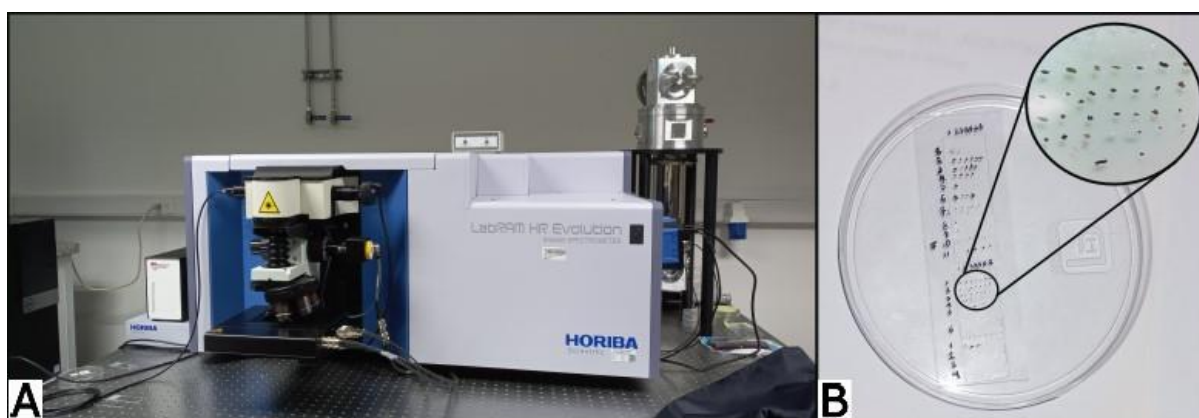
Figure 18. A) LabRam HR Evolution microscope. B) Minerals used.

3.9   X-ray photoelectron spectroscopy (XPS)

A popular technique for determining the chemical composition of surfaces is X-ray Photoelectron Spectroscopy, sometimes referred to as Electron Spectroscopy for Chemical Analysis (ESCA) (Chastain & King,1992). It is one of the most popular methods for surface investigation, and as XPS instrumentation has improved, more researchers are able to employ the method (Stevie & Donley, 2020). XPS has proven to be a potent complement to any analytical laboratory thanks to its capacity to examine the first few atomic layers and assign chemical states to the identified atoms (Chastain & King,1992).

It is a surface-sensitive analytical method that consists in bombards a material surface with X-rays and measures the kinetic energy of the electrons that are released (Stevie & Donley, 2020). This technique allows for obtaining information and a spectrum of almost all chemical elements in a sample or analyzed material. The spectrum is created by plotting the quantity of identified

electrons per energy interval against their kinetic energy (Chastain & King,1992). Thus, X-ray photoelectron spectroscopy allows to obtain a characteristic spectrum for each chemical element. The spectrum of a combination of several chemical elements is roughly equal to the sum of the peaks of its component parts (Chastain & King, 1992).

The analysis of the surface of minerals was carried out using the X-ray photoelectron Spectroscopy (XPS); PHI5000VersaProbe III from Physical Electronics, provided by the laboratory of the School of Physics at Yachay Tech University (Figure 19). The equipment has a monochromatic source of Al Kα for the X-ray source and operates in the pass energy mode at 280 Ev. The size of the analysis points of the different samples was 50 μm in diameter. The detection angle concerning the sample surface was 45°. Atomic concentration was evaluated using Multipak Version 9.8.0.19 software (Ulvac-phi, Inc.). These characteristics are used for the analysis of 9 pulverized fraction, corresponding to the samples MC-05-120, MC-12-120, MC-17-120, each divided to 3 magnetic fractions.

Figure 19. X-ray photoelectron spectroscopy of Yachay Tech University

CHAPTER 4: RESULTS

This chapter show the results of identifying the minerals that compose the fine sediments associated to the CCVC fluvial systems using various physical procedures and analytical techniques.

4.1   Characterization of fluvial sediments

The 22 sand samples analyzed in the present investigation were taken from the sources of high mountain rivers, characterized by the accumulation of gravels and finer sediments on the rocky substrate.

The fraction of gravels is characterized by their red and gray color, either light or dark and angular and subangular shapes (Figure 20A). These materials are shaped in accordance with the direction of erosion, its severity, and the quantity of agents to which they are subjected (Calderón, 2013) including water transport. These clasts of gravels size are possible to distinguish dark minerals with the physical characteristics of amphiboles and light minerals (Figure 20B), such as plagioclase. Thus, the volcanic rocks, which are primarily andesites, dacites, and poorly pumice, were also identified to field, showing concordance with the mentioned in the investigation of Almeida, 2016.

During the fieldwork, it was possible to observe that some tributaries are permanent, with a variable influx of water (Figure 20C). Others are temporary due to recent rains (Figure 20D). Water currents or other factors have allowed the transport of rocks and lithic fragments. However, most of the samples collected have been taken near water sources and have yet to travel long distances.

Figure 20. *Fluvial system associated to CCVC. **A**) Rocks in angular shapes due to little or no transport. B) Lithic fragments mostly red, light and dark gray and angular and subangular shapes. C) Permanent tributaries with variable influx of water. D) Temporary tributaries due to recent rains.*

4.2   Humidity percentage

A time-lapse of 5 days was necessary to complete the sample drying period. The weights obtained after each day of drying transformed into moisture percentages were recorded in Table 3, creating the graph representing the moisture curve of the sample (Figure 20).

Table 3. *Weight percentages obtained with respect to the corresponding seven mesh, after the granulometric separation of the 22 corresponding samples.*

Sample	Initial measure	Day 1		Day 2		Day 3		Day 4		Day 5	
		(g)	%	(g)	%	(g)	%	(g)	%	(g)	%
MC-1	851.83	740.9	13.02	665.1	10.23	647.71	2.61	644.54	0.49	644.4	0.02
MC-2	847.38	787.14	7.11	739.71	6.03	737.73	0.27	737.59	0.02	737.56	0
MC-3	840.03	775.41	7.69	746.01	3.79	744.58	0.19	744.49	0.01	744.46	0
MC-4	950.94	828.79	12.85	766.55	7.51	748.58	2.34	748.26	0.04	748.21	0.01
MC-5	804.69	721.6	10.33	694.6	3.74	693.59	0.15	693.52	0.01	693.51	0
MC-6	850.22	714.09	16.01	664.39	6.96	662.03	0.36	661.94	0.01	661.86	0.01
MC-7	935.12	820.37	12.27	758.28	7.57	740.83	2.3	740.26	0.08	739.93	0.04
MC-8	850.71	735.09	13.59	685.01	6.81	681.54	0.51	681.39	0.02	681.31	0.01
MC-9	672.53	603.16	10.31	561.51	6.91	560.12	0.25	560.01	0.02	559.97	0.01
MC-10	965.51	858.28	11.11	797.9	7.04	768.89	3.64	758.12	1.4	757.93	0.03
MC-11	621.11	593.75	4.41	590.06	0.62	588.63	0.24	588.52	0.02	588.47	0.01
MC-12	805.13	721.14	10.43	655.32	9.13	655.03	0.04	654.72	0.05	654.59	0.02

MC-13	805.56	727.18	9.73	663.23	8.79	663.11	0.02	663.01	0.02	662.95	0.01
MC-14	804.89	713.32	11.38	658.33	7.71	658.05	0.04	657.83	0.03	657.72	0.02
MC-15	805.54	718.85	10.76	665.21	7.46	664.8	0.06	664.54	0.04	664.3	0.04
MC-16	805.65	707.07	12.24	654.72	7.4	654.3	0.06	654.16	0.02	654.09	0.01
MC-17	805.43	705.44	12.41	645.95	8.43	645.55	0.06	645.35	0.03	645.19	0.02
MC-18	805.17	703.24	12.66	643.46	8.5	643.04	0.07	642.92	0.02	642.87	0.01
MC-19	805.25	709.95	11.83	642.81	9.46	642.51	0.05	642.38	0.02	642.21	0.03
MC-20	805.02	655.14	18.62	590.94	9.8	590.62	0.05	590.47	0.03	590.34	0.02
MC-21	805.47	698.18	13.32	662.95	5.05	662.46	0.07	662.18	0.04	662.02	0.02
MC-22	805.33	690.27	14.29	643.92	6.71	643.65	0.04	643.23	0.07	642.98	0.04

The samples humidity values over time are displayed in Figure 21. This figure shows a significant variation in the percentage of humidity of the samples from day 1 to day 3; from day four onwards, the difference in humidity percentage is minimal. The rate of humidity on day 5 varied between 0 and 0.4; this indicates that the samples are sufficiently dry.
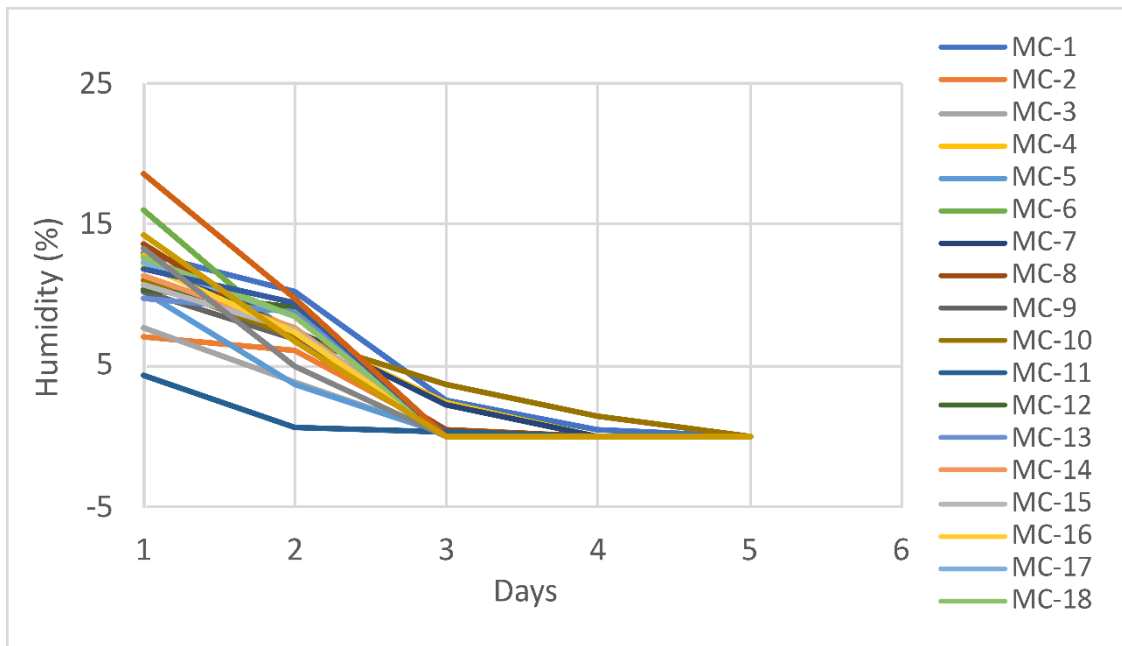
Figure 21. *Experimental plot of the drying process. From day 1 to day 3, it is observed that the humidity percentage of the samples has varied significantly. From day four onwards, the fluctuation is barely noticeable. Finally, on day five, the samples are sufficiently dry.*

4.3   Granulometric percentage

The granulometric separation method of 500 g of the 22 samples allowed the collection of seven fractions from each sample of different sizes (Table 4). The total of the seven fractions of the separate samples varies from 4.9 g to 3206.41 g in weight, equivalent to 0.04 and 29.25% of the total of the samples (Table 4). The most representative fractions are those collected in the 35, 60, and 120 mesh, where 3206.41, 2730.21, and 2840.49 g were collected respectively

from 22 samples (Table 4), equivalent to 29.5% of the sample collected on the 35 mesh, 24.92% of the sample collected on the 60 mesh, and 25.94% of the sample collected on the 120 mesh (Table 4). These are the most representative fractions that will be taken for the following procedure.

Table 4. *Weight and percentages obtained from the granulometric separation of 22 samples in 7 sieves.*

| Sample | Grams of samples collected from the mesh of sieves: | | | | | | | | | | | | | | Sum | |
| | 10 (2 mm) | | 18 (1 mm) | | 35 (0.5 mm) | | 60 (0.25 mm) | | 120 (0.125 mm) | | 230 (0.063 mm) | | <230 (rest) | | | |
	(g)	%	(g)	%	(g)	%	(g)	%	(g)	%	(g)	%	(g)	%	(g)	%
MC-1		0	52.8	10.58	178.04	35.67	143.95	28.84	108.04	21.64	12.1	2.42	4.23	0.85	499.16	100
MC-2		0	166.34	33.35	215.62	43.23	85.72	17.19	25.84	5.18	2.7	0.54	2.57	0.52	498.79	100
MC-3	0.1	0.02	102.84	20.61	192.99	38.68	117.15	23.48	79	15.83	5.46	1.09	1.45	0.29	498.89	100
MC-4		0	59.85	12.04	137.05	27.57	137.05	27.57	140.54	28.27	19.79	3.98	2.79	0.56	497.07	100
MC-5		0	57.25	11.53	141.03	28.41	134.72	27.14	149.07	30.03	12.69	2.56	1.58	0.32	496.34	100
MC-6		0	110.55	22.16	209.89	42.07	116.17	23.29	53.2	10.66	5.23	1.05	3.85	0.77	498.89	100
MC-7	3.24	0.65	125.48	25.09	156.55	31.3	88.87	17.77	82.45	16.49	24.54	4.91	18.95	3.79	496.84	100
MC-8	1.22	0.24	173.8	34.9	170.91	34.32	80.21	16.11	53.63	10.77	9.21	1.85	8.98	1.8	496.74	100
MC-9	0.34	0.07	121.96	24.51	174.38	35.05	106.34	21.37	80	16.08	10.2	2.05	4.31	0.87	497.19	100
MC-10		0	88.18	17.7	130.79	26.26	101.58	20.39	126.77	25.45	39.09	7.84	11.75	2.36	498.16	100
MC-11		0	12.39	2.49	199.99	40.15	223.29	44.82	61.5	12.35	0.62	0.12	0.35	0.07	498.14	100
MC-12		0	78.9	15.87	122.94	24.72	101.51	20.41	153.38	30.84	31.29	6.29	9.3	1.87	497.32	100
MC-13		0	111.47	22.37	190.65	38.26	90.52	18.17	73.11	14.67	19.15	3.84	13.37	2.68	498.27	100
MC-14		0	35.17	7.05	139.82	28.03	158.9	31.85	152.89	30.65	11.13	2.23	0.92	0.18	498.83	100
MC-15		0	84.28	16.87	202.23	40.48	120.64	24.15	77.96	15.61	8.58	1.72	5.86	1.17	499.55	100
MC-16		0	46.45	9.35	113.07	22.76	98.73	19.87	188.65	37.97	43.29	8.71	6.68	1.34	496.87	100
MC-17		0	2.13	0.43	27.41	5.55	111.65	22.59	294.02	59.48	49.23	9.96	9.87	2	494.31	100
MC-18		0	30.36	6.11	125.74	25.29	129.54	26.05	127.32	25.61	51.69	10.4	32.54	6.54	497.19	100
MC-19		0	23.83	4.78	126.09	25.32	159.13	31.95	162.2	32.57	19.85	3.99	6.95	1.4	498.05	100
MC-20		0	35.76	7.19	144.56	29.05	135.41	27.21	145.73	29.28	24.67	4.96	11.55	2.32	497.68	100
MC-21		0	12.31	2.47	60.4	12.11	159.03	31.88	246.5	49.41	18.21	3.65	2.42	0.49	498.87	100
MC-22		0	2.62	0.53	46.26	9.29	130.1	26.13	257.69	51.76	50.08	10.06	11.12	2.23	497.87	100
Sum (g)	4.9	0.98	1534.72	307.98	3206.41	643.56	2730.21	548.23	2840.49	570.61	468.8	94.22	171.39	34.42	10956.92	2200
%		0.04		14		29.25		24.92		25.94		4.28		1.56		100

The particle size fractions of each sample are shown in Figure 22, where it can be easily seen that the most abundant fractions correspond to the 35, 120 and 60 mesh. In contrast, the fractions collected at mesh 10, 18, 230, and <230 have the low percentages.
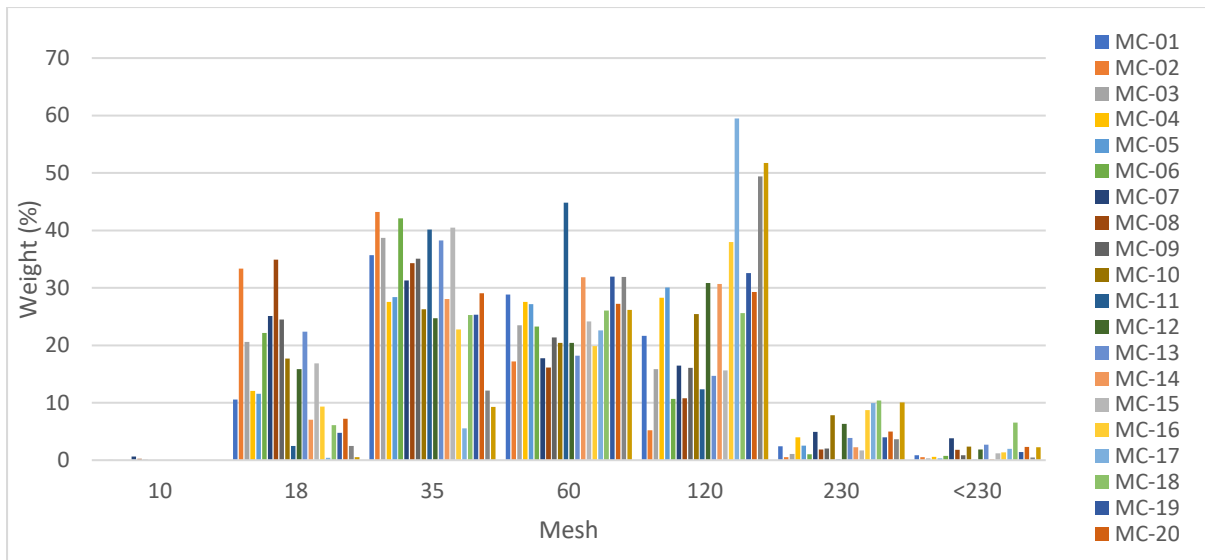
Figure 22. Representation of the percentage of the results of the particle size separation of 22 samples in seven mesh sizes. The bars in the image represent the weight percentage of each sample collected in the seven mesh. It clearly shows higher percentages of samples collected in the 35, 120, and 60 mesh. The fractions collected at mesh 18 have intermediate percentages. In contrast, the fractions collected at mesh 10, 230, and <230 have the lowest percentages.

4.4   Mineralogical characterization by stereomicroscopy

The stereomicroscopic observation of the three fractions collected in the 35 (Figure 23A), 60 (Figure 23B), and 120 mesh (Figure 23C), of the samples MC-01, MC-05, MC-09, MC-12, MC-14, MC-17, and MC-20, it was possible to identify lithics and minerals. These lithics are found in all three examined fractions, but the amount of lithics reduces as the sieve opening diameter decreases. The lithic fragments correspond to andesite, dacite and pumice rocks. The lithics are mainly in angular and subangular shapes and mostly reddish and gray colors. According to the tectonic and sedimentary context of the rock's evolution, as well as its geological history, the mineralogy and shape of these granules will vary, adapting the mineral granules texture to the stresses that the rock itself experiences (Calderon, 2013).

Figure 23. A) Fraction collected at 35 mesh with a high presence of lithic fragments and almost no minerals. B) Fraction collected at 60 mesh with high presence of lithic fragments and little presence of minerals. C) Fraction collected at 120 mesh with little presence of lithic fragments and high presence of minerals.

30

The physical characteristics of the minerals allowed the identification of four different groups of minerals: plagioclase (plag), pyroxene (pyx), amphibole (amp), and two iron oxides; magnetite (mag) and hematite (hem).

Plagioclase mineral grains, in particular, are transparent and in anhedral forms (Figure 24A, 25). The most relevant characteristics of pyroxenes identified are their green and transparent brown color and orthorhombic shape (Figure 24B, 25). The amphiboles mineral granules have a dark color and elongated and prismatic shapes; it is also possible to easily see cleavage in some minerals (Figure 24C, 25). The magnetite is characterized by its metallic luster and black color, octahedron shape, and flat faces (Figure 24D, 25). They are also shown to be smaller than the other minerals collected on the same mesh. The hematite mineral grains occur particularly in red and small amounts in black color and amorphous anhedral forms (Figure 24E, 25).
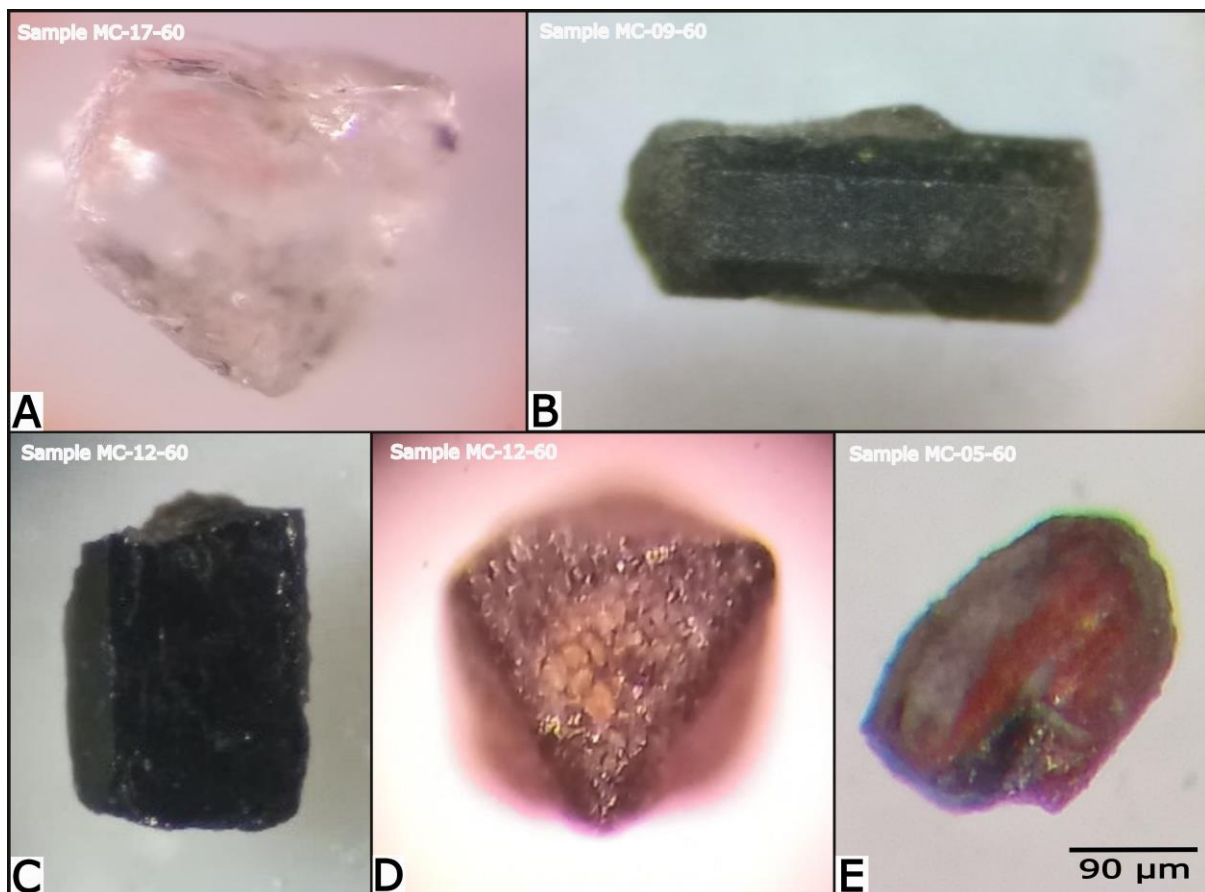
Figure 24. A) An angular and translucent plagioclase mineral grain. B) Green pyroxene mineral grain sample with an orthorhombic form. C) Amphibole mineral grain of black color and elongated and prismatic form. E) Magnetite mineral grain with flat faces, octahedron shape, and metallic luster. D) Hematite mineral grain is primarily red and black with an amorphous shape. Scale is the same for all images.

The mineral grams with the physical characteristics that differentiate the minerals mentioned above are repeated in the seven samples analyzed. Some examples have been isolated and photographed (Figure 25).
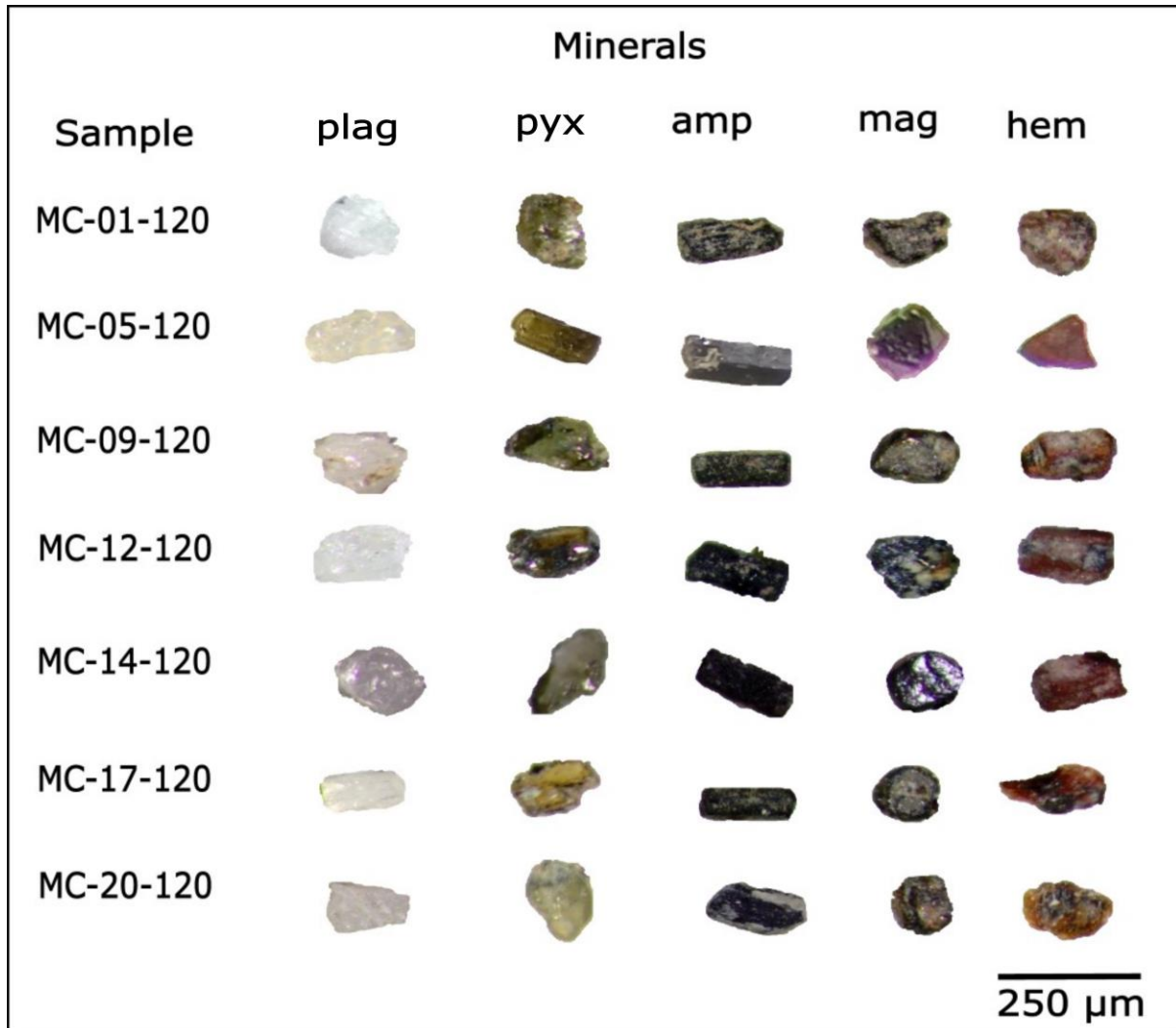
Figure 25. *Minerals identify in samples MC-01, MC-05, MC-09, MC-12, MC-14, MC-17, MC-20. Legend: Pyroxene (pyx), Hematite (hem), Magnetite (mag), Plagioclase (plag) and Amphibole (amp).*

After looking at the three fractions gathered on the 35, 60, and 120 mesh of the seven samples chosen at random. It was possible to determine that the fraction collected at 120 mesh is the most suitable for Raman spectroscopy, XRD, and XPS analysis. Minerals of this fraction make up 92.1% of the entire fraction, with the remaining 7.9% comprising lithic fragments (Figure 26). In contrast, the fraction collected in the 60 mesh has 45.77% of minerals and 54.23% of lithics fragments, and the fraction contained in the 35 mesh presents 24.74% of minerals and 75.26% of lithics fragments.
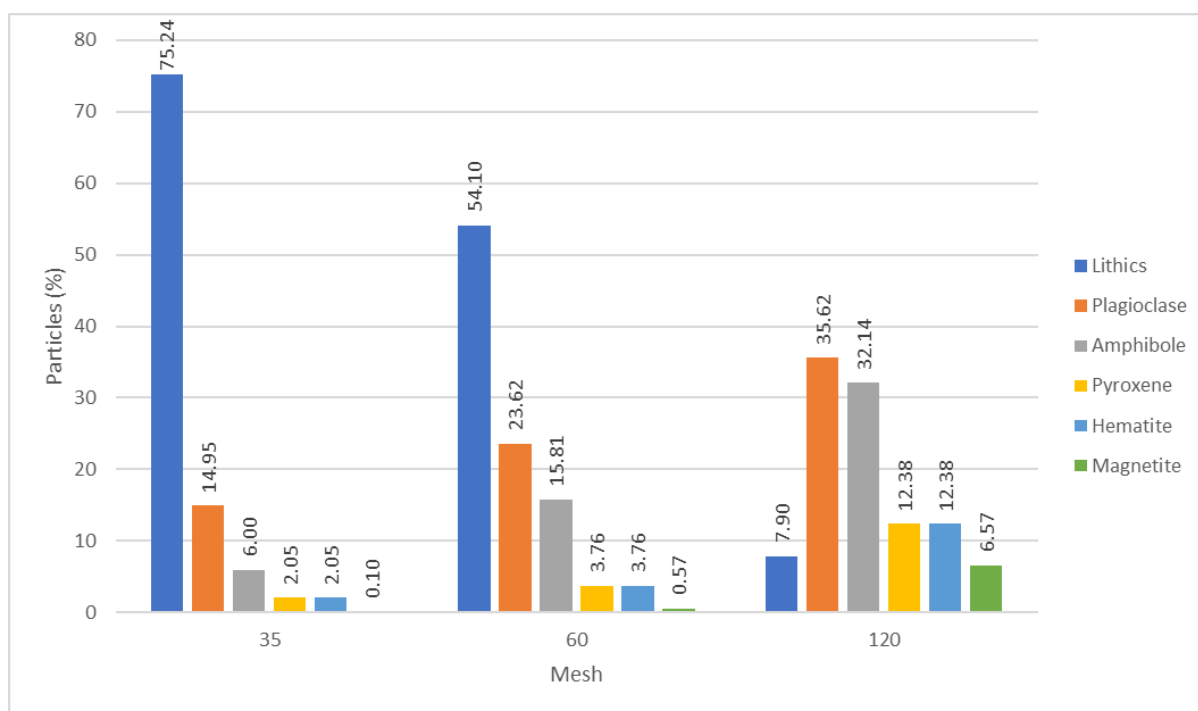
Figure 26. *Percentages resulting from mineral and lithic counts of the sample collected on the 35, 60 and 120 mesh. The fraction collected in 120 mesh has the highest number of minerals, its presents 92.1% of minerals and 7.9% of lithics fragments. In contrast, the fraction collected in the 60 mesh has 45.77% of minerals and 54.23% of lithics fragments, and the fraction contained in the 35 mesh presents 24.74% of minerals and 75.26% of lithics fragments.*

Since the fraction collected in the 120 mesh has the highest number of minerals, the percentage of minerals in each analyzed sample was calculated. In samples MC-01-120 and MC-09-120, it was possible to identify that plagioclase is the most abundant mineral, followed by amphibole, pyroxene, hematite, and finally, magnetite, which is the least abundant mineral (Table 5). In sample MC-05-120, it was possible to identify that plagioclase and amphibole are found in equal amounts, followed by pyroxene, magnetite, and hematite in smaller quantities (Table 5). In samples MC-12-120 and MC-14-120, it is recognizable that amphibole is the most abundant mineral, followed by plagioclase, pyroxene, magnetite, and finally, the least abundant mineral, hematite (Table 5). Also, in samples MC-17-120 and MC-20-120, it was possible to identify plagioclase as the most abundant mineral, followed by amphibole, pyroxene, magnetite, and hematite as the least abundant mineral (Table 5).

Table 5. *Lithics and particular mineral particle percentages determined by stereomicroscopic observations*

Sample	Particles (%)					
	Lithics	Plag	Amp	Pyx	Hem	Mag
MC-01-120	20.33	30.67	23.33	18.33	6	1.33
MC-05-120	2.67	39.67	39.67	9.67	4	4.33

MC-09-120	12.67	30.67	26.33	11.67	10.33	8.33
MC-12-120	4	34.67	40.67	10.33	2.33	8
MC-14-120	1.67	36	37.33	10	6.33	8.67
MC-17-120	1.67	38.67	33.33	4	4	9.33
MC-20-120	12.33	39	24.33	13.67	4.67	6

4.5   Magnetic separation

The samples collected to 120 mesh were divided by their magnetic properties into three fractions: magnetic (Figure 27A), low-magnetic (Figure 27B), and non-magnetic (Figure 27C). In some cases, there are a contamination of grain minerals that not correspond to each fraction. Figure 27 shows low-concentration mineral particles that do not belong to the respective fraction. The magnetic fraction is dominated by magnetite and hematite. However, it is also possible to find small fragments of plagioclase. There are amphiboles, pyroxenes, and only a few plagioclases mineral grains in the low-magnetic fraction. In the non-magnetic fraction, plagioclase predominates. However, it is also possible to find some pyroxene and amphibole minerals, either loose or attached to plagioclase.

Figure 27. *Imagines of result of magnetic separation of fraction collected 0f mesh 120 of sample MC-17. A) Magnetic fraction separates to magnitude of 0,35. B) Medium fraction separate to magnitude of 0,2. A) No magnetic fraction separate to magnitude of 0,35.*

Magnetic separation also allowed us to determine the weight percentage of each magnetic. This yielded representative results for the magnetic and non-magnetic fractions. The magnetic fraction, whose weight percentages from 43.14 to 77.64, is the most representative fraction (Table 6). The low magnetic fraction, which is the least representative, has percentages from 7.19 to 19.91 (Table 6). The non-magnetic proportion ranges from 12.80 to 43.70% (Table 6). Thus, the magnetic fraction represents 59.05% of the total mass of all samples, the low magnetic fraction 13.40%, and the non-magnetic fraction 27.55% (Table 6).

Table 6. The table shows the percent abundances of the three magnetically separated fractions.

Samples	Weight percentages		
	Magnetic (%)	Low-magnetic (%)	Non-magnetic (%)
MC-1	63.73	9.92	26.36
MC-2	66.54	10.87	22.58
MC-3	65.96	13.77	20.27
MC-4	49.2	16.36	34.44
MC-5	57.62	15.04	27.34
MC-6	54.77	14.97	30.25
MC-7	57.04	14.38	28.58
MC-8	53.68	14.74	31.58
MC-9	72.82	10.02	17.16
MC-10	49.09	11.76	39.15
MC-11	77.64	8.33	14.02
MC-12	58.69	16.57	24.74
MC-13	80.01	7.19	12.8
MC-14	50.03	18.91	31.06
MC-15	60.63	15.28	24.09
MC-16	60.92	14.45	24.63
MC-17	56.04	16.01	27.95
MC-18	60.97	14.43	24.6
MC-19	63.85	10.18	25.97
MC-20	65.72	14.1	20.17
MC-21	68.95	8.11	22.94
MC-22	43.14	13.15	43.7
% total mass	59.05	13.4	27.55

4.6   Mineralogical characterization by X-Ray Diffraction

A total of 7 samples divided into three magnetic fractions each were analyzed by XRD. This analysis identified plagioclase in the non-magnetic fraction, amphiboles in the low-magnetic fraction, and iron oxides in the magnetite fraction (Table 7). Among the feldspars, two types of plagioclases were recognized: labradorite and andesine. Hornblende from the amphibole group and from the iron oxides group, magnetite, was distinguished. The mineral phases have been determined by comparing the experimental spectrum (blue lines) with the database spectrum (red lines). However, finding some of the minerals found in the previous analysis, such as pyroxenes and hematite, was impossible.

Sample	Fraction	Mineral Phase			
		Non-magnetic fraction		Low-magnetic fraction	Magnetic fraction
		Feldspar-Plagioclase		Amphibole	Iron Oxide
		Lab	Ads	Hrb	Mag
MC-01-120	Magnetic				x
	Low-magnetic			x	
	Non-magnetic	x			
MC-05-120	Magnetic				x
	Low-magnetic			x	
	Non-magnetic	x			
MC-09-120	Magnetic				x
	Low-magnetic			x	
	Non-magnetic		x		
MC-12-120	Magnetic				x
	Low-magnetic			x	
	Non-magnetic		x		
MC-14-120	Magnetic				x
	Low-magnetic			x	
	Non-magnetic	x			
MC-17-120	Magnetic				x
	Low-magnetic			x	
	Non-magnetic	x			
MC-20-120	Magnetic				x
	Low-magnetic			x	
	Non-magnetic	x			

4.6.1 Plagioclase

The *labradorite* was one of the more prevalent minerals identified during the DRX analyses. This mineral was present in almost all the non-magnetic fractions of the seven samples examined. The experimental spectra from the MC-01-120-N, MC-05-120-N, MC-14-120-N, MC-17-120-N, and MC-01-120-N show peaks with a high coincidence rate, particularly at 2θ between 20° to 35.20°. They were especially presenting the peak of higher coincidence located at 2θ=28°. We may see an example taken from the MC-01-120-N exhibit in Figure 28.
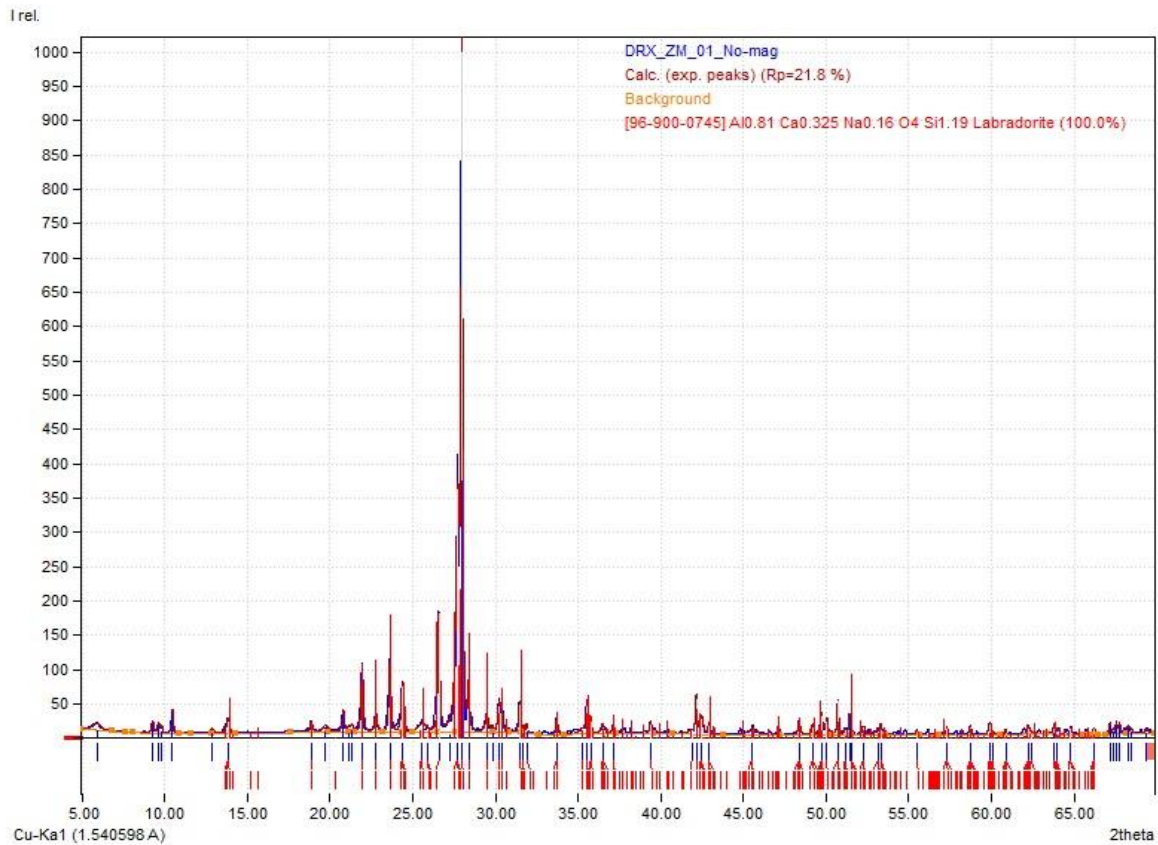
Figure 28. *Spectrum resulting from XRD analysis of the non-magnetic fraction of sample 01, where the presence of labradorite is clearly indicated. It shows peak of higher coincidence located at 2θ=28° and others with less intensity at 2θ between 20° to 35.20°.*

Experimental spectra from the MC-09-120-N and MC-14-120-N samples showed strong similarities to those of the *andesine* database. It shows peaks of higher coincidence at 2θ between 20° and 35°. Figure 29, taken from the sample MC-09-120-N, shows how the experimental and database spectral lines coincide, especially in the peaks located at 2θ=28°.
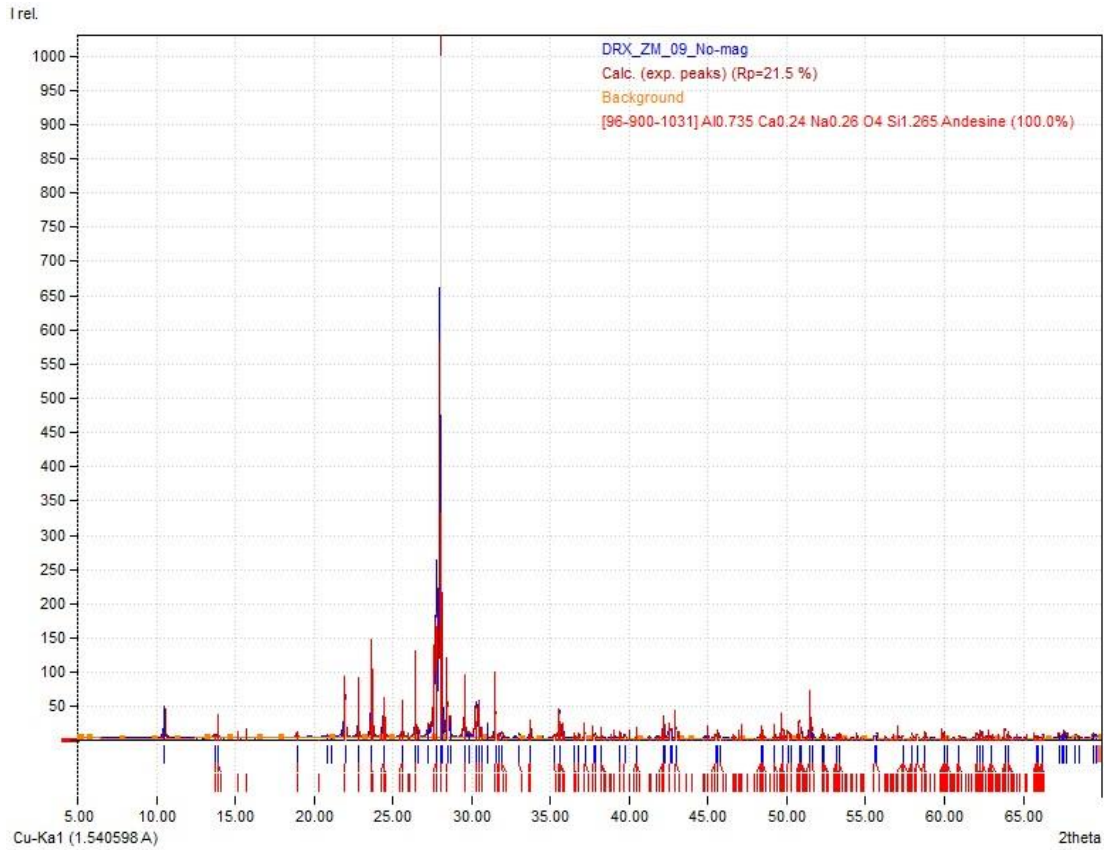
Figure 29. *Spectrum resulting from XRD analysis of the non-magnetic fraction of sample 09. The spectrum shows peak of higher coincidence located at 2θ=28° and others with less intensity at 2θ between 20° to 35.20°. The spectrum indicates the presence of andesine.*

4.6.2 Amphibole

Experimental spectra from the seven low-magnetic fractions analyzed showed strong similarities to those of the *hornblendes* database. The most notable coincidence peaks at 2θ=11°. Additionally, several less-pronounceable peaks are in the 2θ at 27° to 35°. Figure 30, taken from the sample MC-12-120-N, shows how the experimental and database spectral lines coincide.
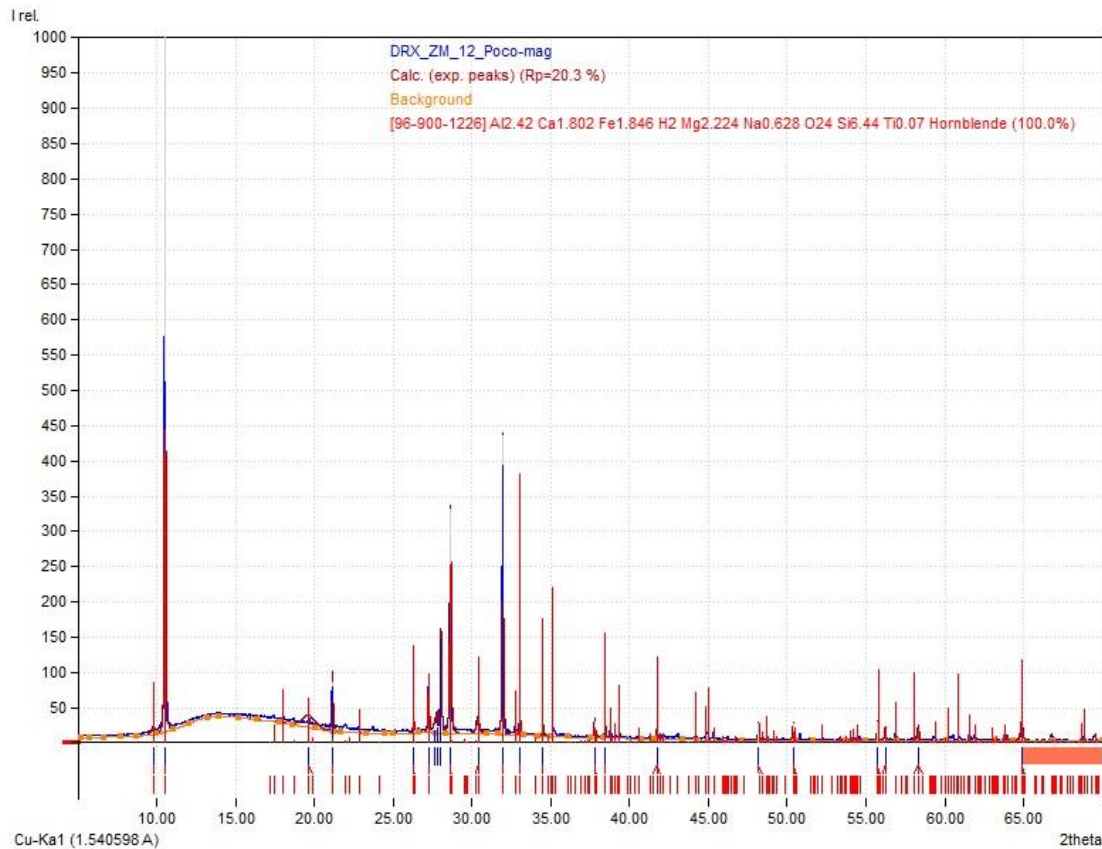
Figure 30. *Spectrum resulting from XRD analysis of the non-magnetic fraction of sample 12, the most notable peak at 2θ=11°. Additionally, several less-pronounceable peaks are in the 2θ at 27° to 35°. The spectrum indicates the presence of hornblende.*

4.6.3 Iron Oxides

Magnetite is present in all the magnetic fractions analyzed. Found a significant coincidence in the peaks located at 2θ=28°, 31°, 35°, 44°, 54°, 57°, and 62°. Figure 31, which is taken from the analysis of the sample MC-05-120-N, illustrates this.
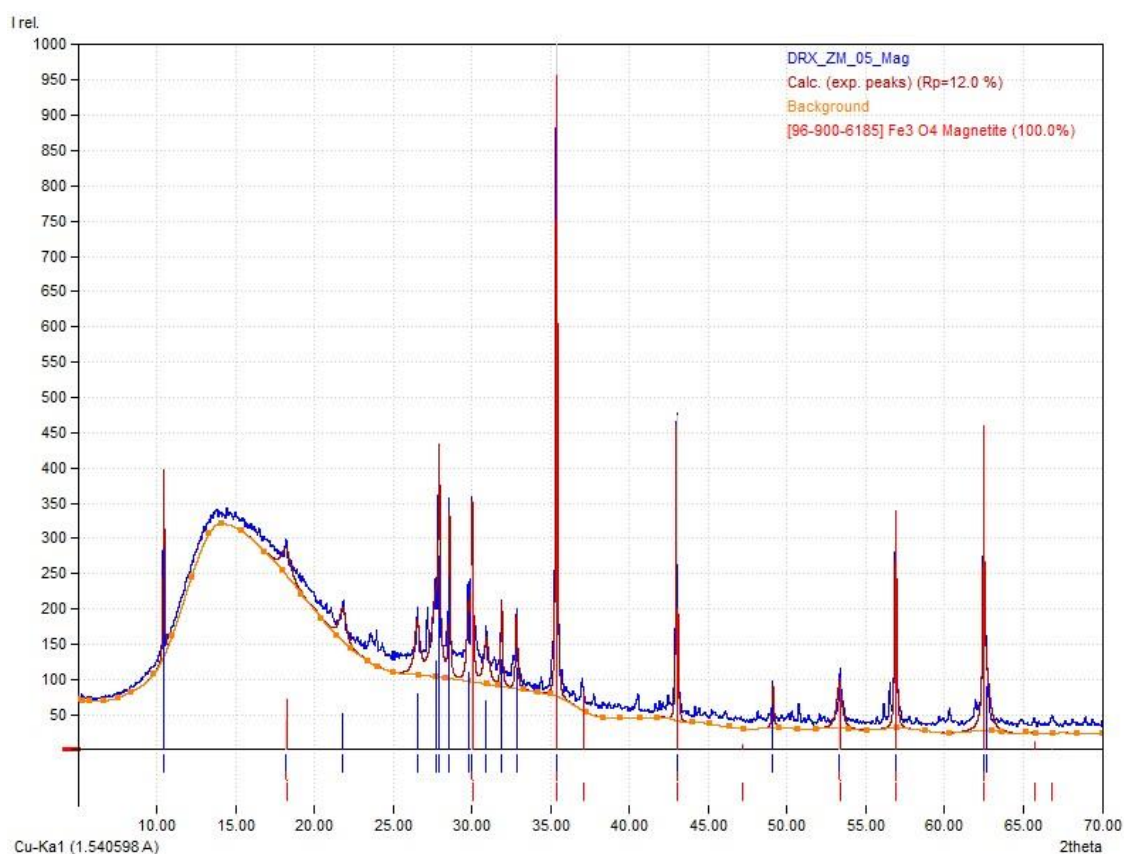
Figure 31. *Spectrum resulting from XRD analysis of the non-magnetic fraction of sample 05, where the presence of magnetite is clearly indicated. The spectrum shows peaks of higher coincidence located at 2θ=28°, 31°, 35°, 44°, 54°, 57°, and 62°.*

4.7   Mineralogical Characterization by Raman Spectroscopy

Raman Spectroscopy analysis has allowed us to identify some minerals that previous analysis could not identify. It has also allowed to know the specific name of the minerals since Raman spectroscopy works with individual particles, so in this case, the quantity of minerals in each sample is irrelevant. Additionally, according to the stereomicroscope observations, all samples have the same minerals; this analysis focuses on just one sample. Choose the minerals to be analyzed from sample MC-05 collected at 120 mesh since this sample contains very clear and loose minerals without matrix residues or other materials. Identified eight minerals and classified them into plagioclase, pyroxenes, amphiboles, and iron oxides. The non-magnetic fraction revealed the presence of two plagioclases: labradorite and andesine. The low-magnetic fraction contained pyroxene and amphibole, enstatite and augite in pyroxene, and magnesio-hastingsite in amphibole. Finally, Magnetite and hematite are two iron oxides in the magnetic fraction. The minerals have been identified by comparing the experimental spectrum with the RRUFF database spectrum.

4.7.1 Plagioclase

Figure 32 shows an example of the *labradorite* mineral grain (Figure 32A), Raman photo (Figure 32B), and experimental (blue) and RRUFF database labradorite spectrum (black) (Figure 32C). The experimental spectrum compared with the spectra from the RRUFF database shows a high coincidence with Labradorite. The percentage of coincidence is 87% in the approximate range of -14 to 1995 cm^{-1}. The most characteristic peaks are 5, 91, 178, 281, 510, 1280, 1453, 1616, and 1885 cm^{-1}. Examined six minerals with similar physical characteristics of plagioclase were analyzed and their spectra were nearly identical.
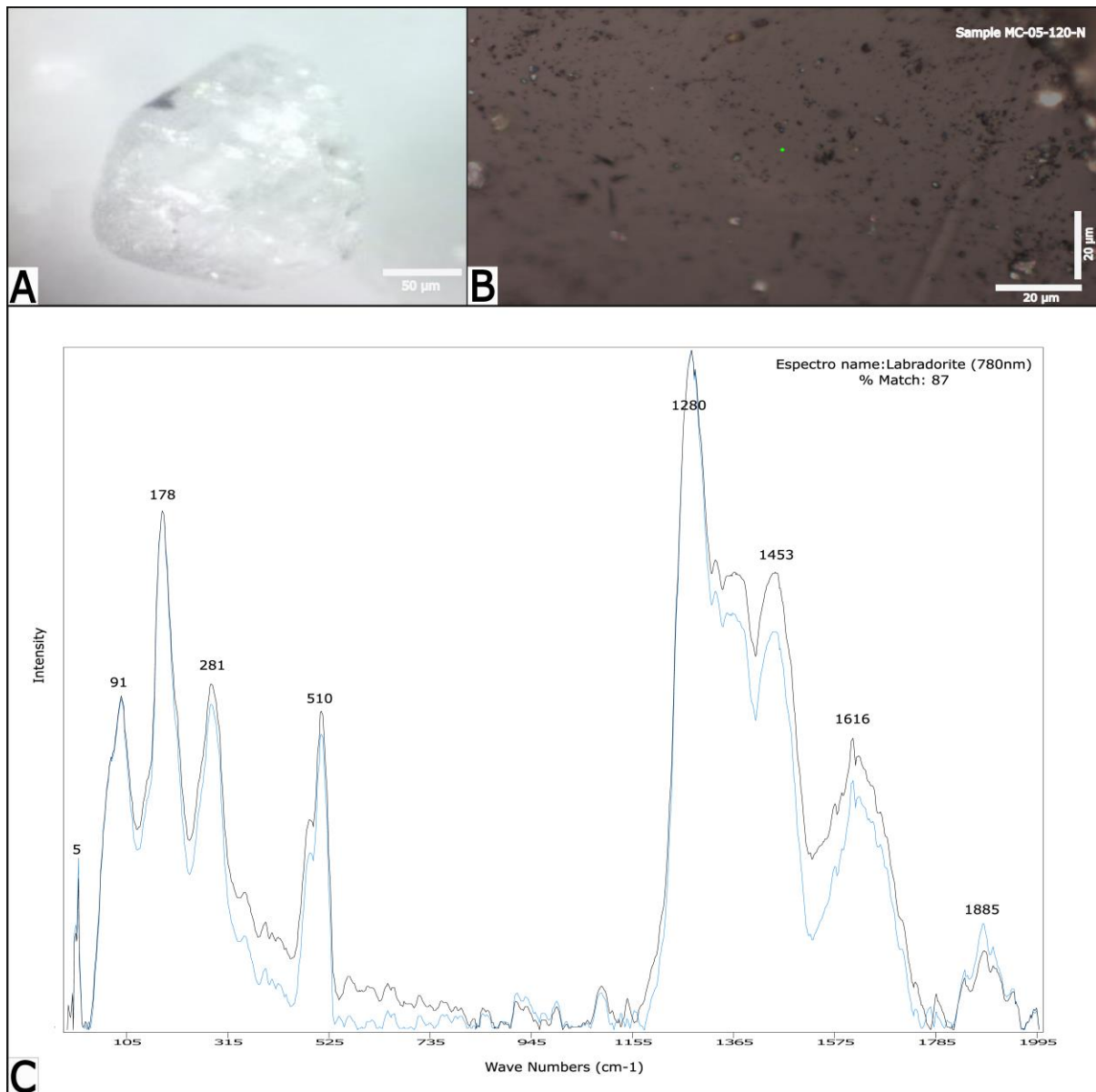
Figure 32. A) The mineral grain whit physic characteristics of labradorite. B) Raman photo. C) Spectra Raman. The RRUFF database of labradorite (black) show a match of 87% in the approximate range of -14 to 1995 cm^{-1}. The most characteristic peaks are 5, 91, 178, 281, 510, 1280, 1453, 1616, and 1885 cm^{-1}.

At least two mineral grains with characteristics of an *andesine* were analyzed, all of which gave us spectra similar to that of the RRUFF database. Figure 33 shows an example of the mineral grain (Figure 33A), Raman photo (Figure 33B), and experimental (blue) and RRUFF database andesine spectrum (black) (Figure 33C). Comparing the experimental spectrum with the RRUFF database of Andesine, a significant coincidence is found in the approximate range of 230 to 1480 cm^{-1}. Well-defined peaks are located at 5, 91, 178, 281, 510, 1280, 1453, 1616, and 1885 cm^{-1}. Additionally, the andesine Raman spectrum is not directly included in the data base that the software CrystalSleuth uses in this case, making it impossible to obtain the coincident percentage.
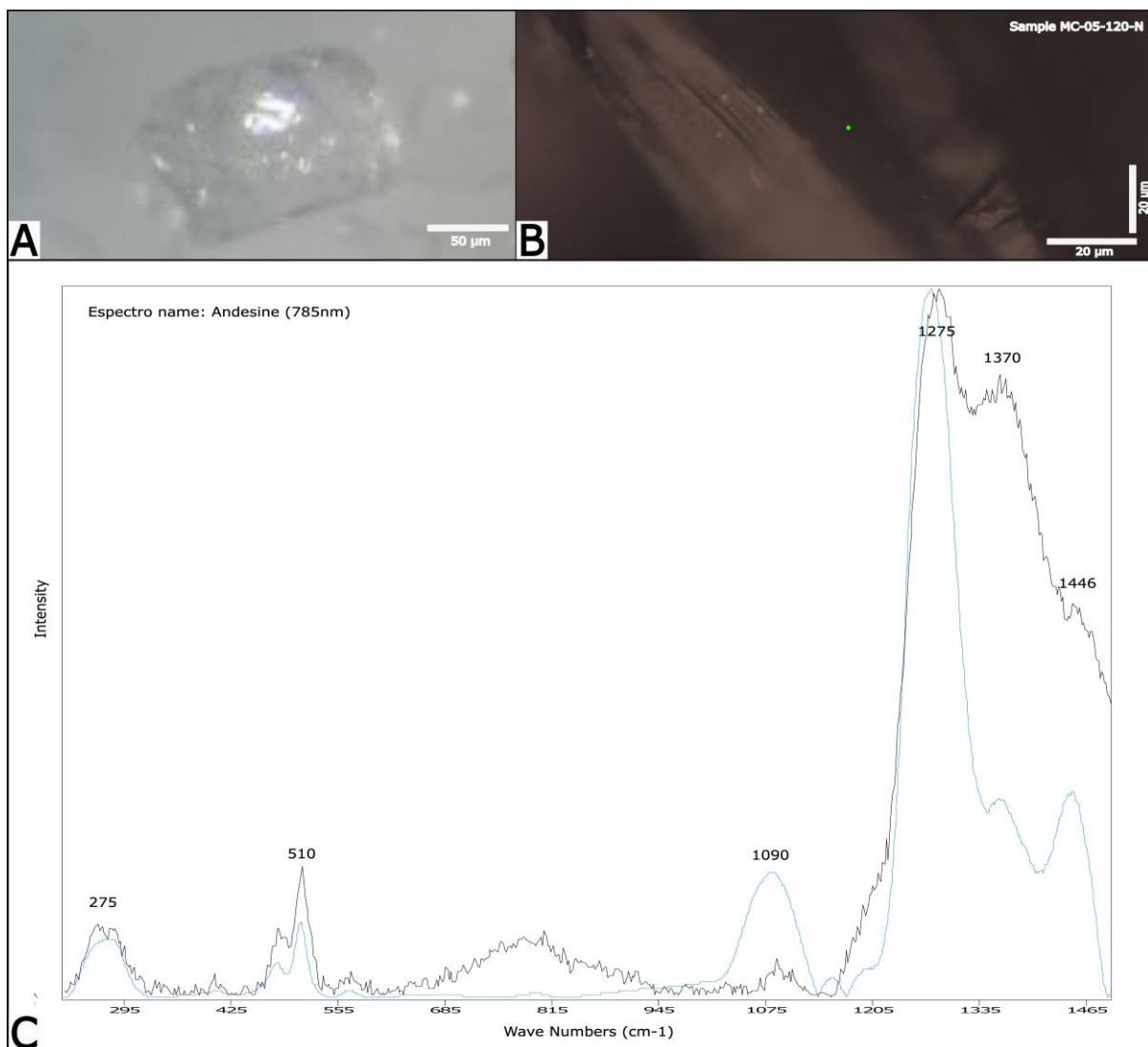
Figure 33. A) The mineral grain whit physic characteristics of andesine. B) Raman photo. C) Spectra Raman. The experimental spectrum (blue) and the RRUFF database of Andesine (black), show a significant coincidence in the approximate range of 230 to 1480 cm^{-1}. Well-defined peaks are located at 5, 91, 178, 281, 510, 1280, 1453, 1616, and 1885 cm^{-1}.

4.7.2 Pyroxene

Figure 34 shows an example of the *enstatite* mineral grain (Figure 34A), Raman photo (Figure 34B), and experimental (blue) and RRUFF database enstatite spectrum (black) (Figure 34C). The experimental spectrum obtained from the analysis of one mineral grain agrees 90% with the RRUFF database spectrum of the mineral enstatite. The spectrum agrees, especially in the intervals from 300 to 1270 cm^{-1} approximately, and the prominent peaks are found at 338, 658, 680, and 1012 cm^{-1}. At least six minerals of similar physical characteristics of pyroxene were analyzed, all of which yielded identical spectra.
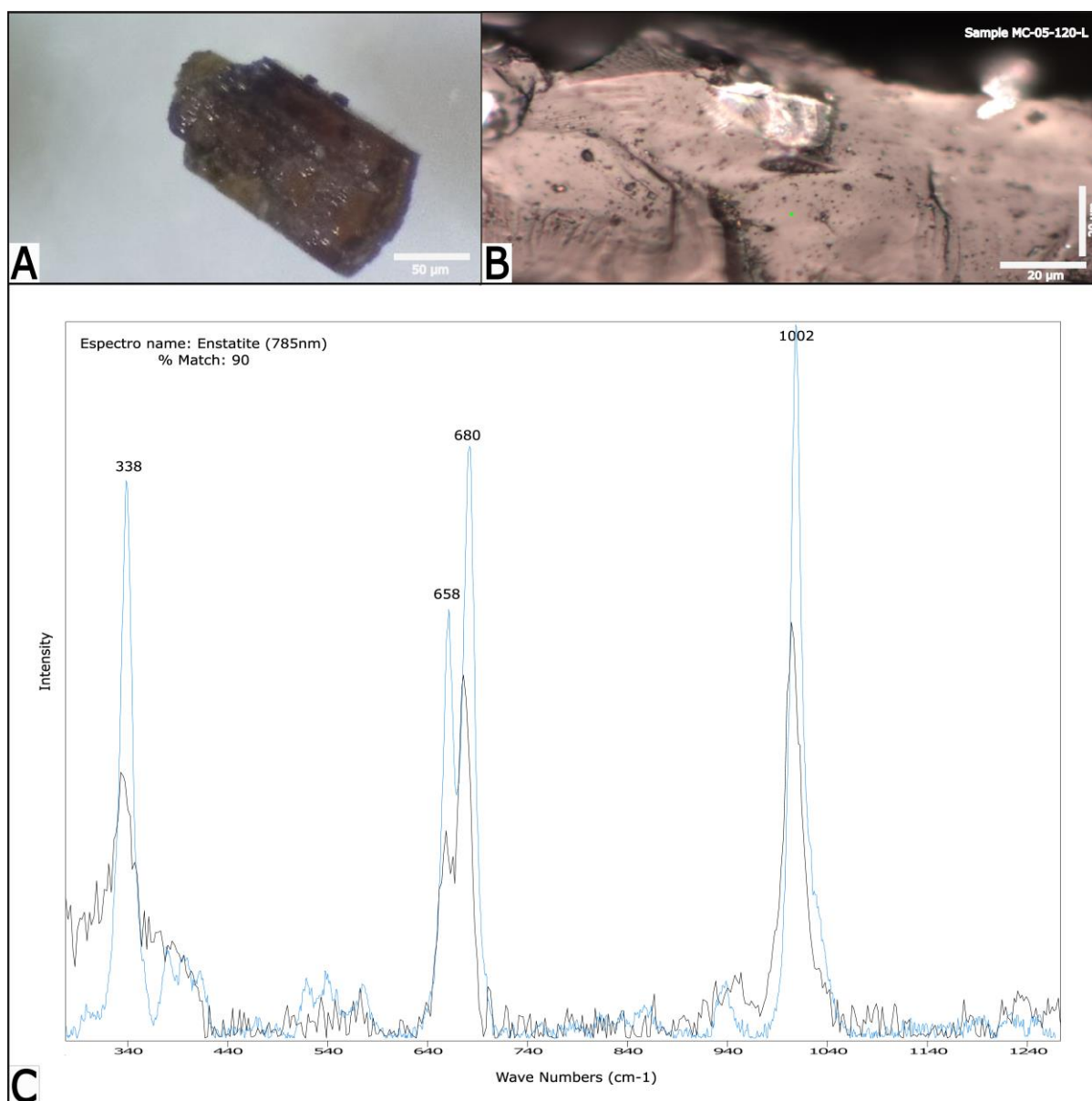
Figure 34. A) The mineral grain whit physic characteristics of enstatite. B) Raman photo. C) Spectra Raman. The experimental (blue) and RRUFF data base of enstatite (black)spectrum show a match of 90 % in the intervals from 300 to 1270 cm^{-1} approximately, and the prominent peaks are found at 338, 658, 680, and 1012 cm^{-1}.

An example of *augite* mineral grain (Figure 35A), Raman photo (Figure 35B), and experimental (blue) and RRUFF database augite spectrum (black) (Figure 35C) are shown in Figure 35. The augite was recognized mainly by coincidence peaks at 60, 140, 186, 326, 390, 513, 665, and 1010 cm^{-1}. The experimental spectrum with that of the RRUFF database coincides with 92% in the 54 to 1995 cm^{-1} range. At least seven satisfactory augite spectra were obtained.
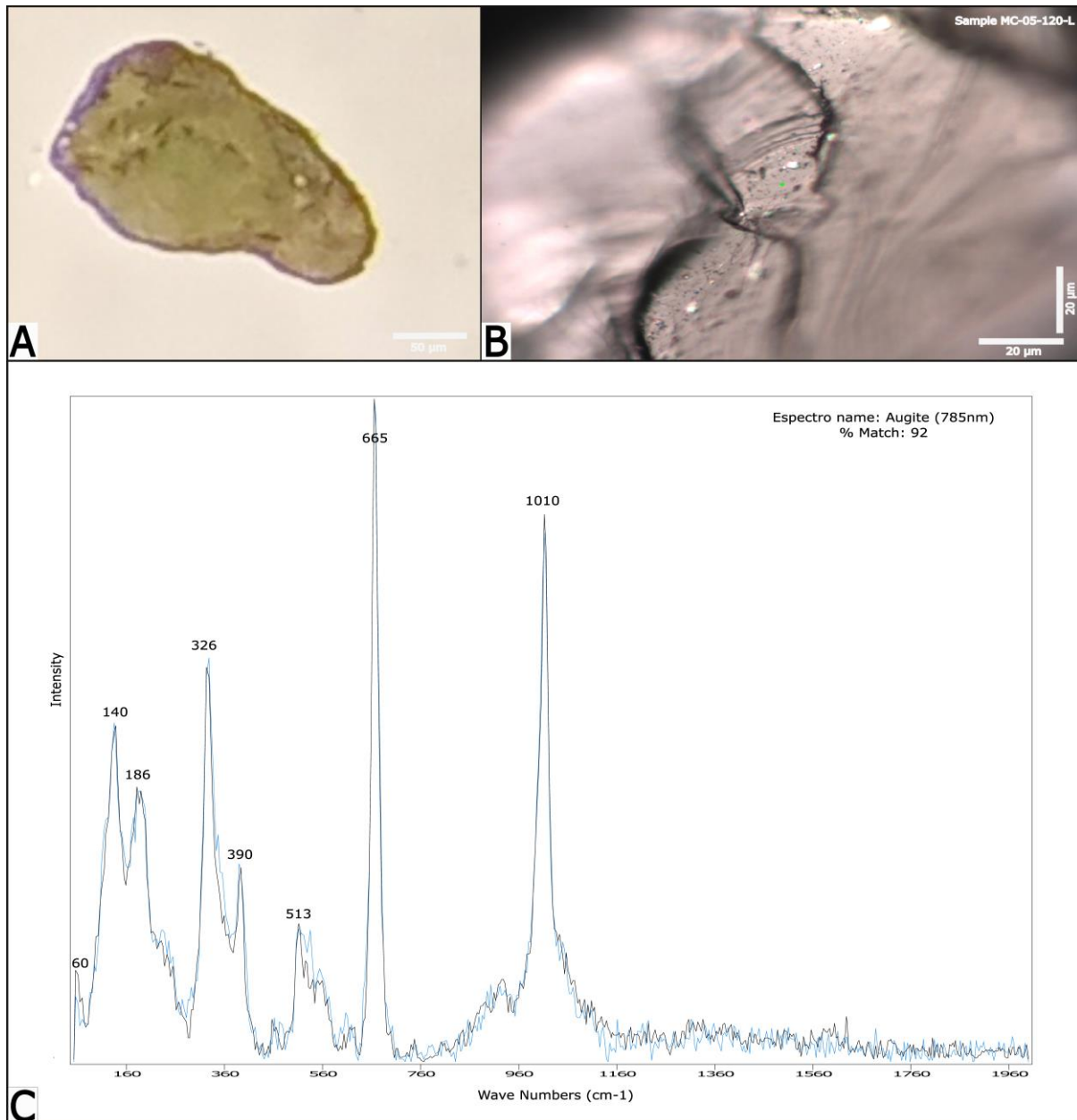
Figure 35. A) The mineral grain whit physic characteristics of augite. B) Raman photo. C) Spectra Raman. The experimental spectrum (blue) with that of the RRUFF database of augite (black) show match of 92% in the 54 to 1995 cm^{-1} range. The spectra show pronounced peaks at 60, 140, 186, 326, 390, 513, 665, and 1010 cm^{-1}.

4.7.3 Amphibole

At least six spectra were compared, and all showed satisfactory coincidence results with the mineral *magnesio-hastingsite*. Figure 36 shows an example of the mineral grain (Figure 36A), Raman photo (Figure 36B), experimental (blue), and RRUFF database magnesio-hastingsite spectrum (black) (Figure 36C). Compared with the RRUFF database, the experimental spectrum has a 92% coincidence with the taramite. Its percentage of coincidence is in the range of 260 to 1200 cm^{-1}, and its characteristic peaks are found in the values 370, 528, 665, and 1000 cm^{-1}.
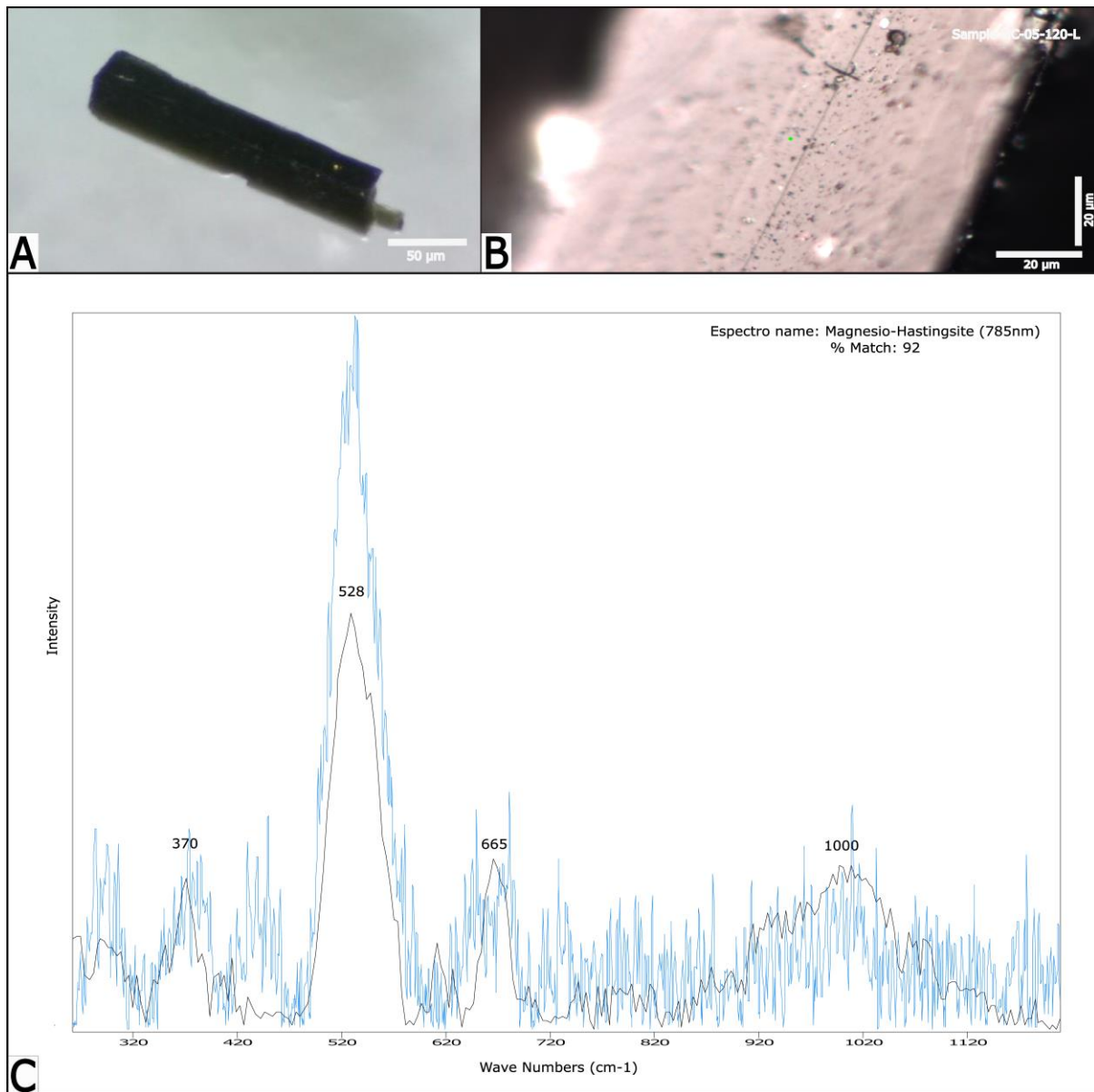
Figure 36. *A) The mineral grain whit physic characteristics of magnesio-hastingsite. B) Raman photo. C) Spectra Raman. The RRUFF database of taramite (black), and the experimental spectrum (blue) has a 91% coincidence with the taramite in the range of 260 to 1200 cm^{-1}, and its characteristic peaks are found in the values; 370, 528, 665, and 1000 cm^{-1}.*

4.7.4 Iron Oxide

At least six mineral grains with characteristics of magnetite were analyzed, all of which gave us spectra similar to that of the RRUFF *magnetite* database. For example, the mineral grain (Figure 37A), Raman photo (Figure 37B), and experimental (blue) and RRUFF database magnetite spectrum (black) (Figure 37C) are shown in Figure 37. The obtained experimental spectrum, when compared with the spectrum of magnetite from the RRUFF database, shows an 82% match in the range from 450 to 1257 cm^{-1}. This spectrum only has a characteristic peak at approximately 683 cm^{-1}.
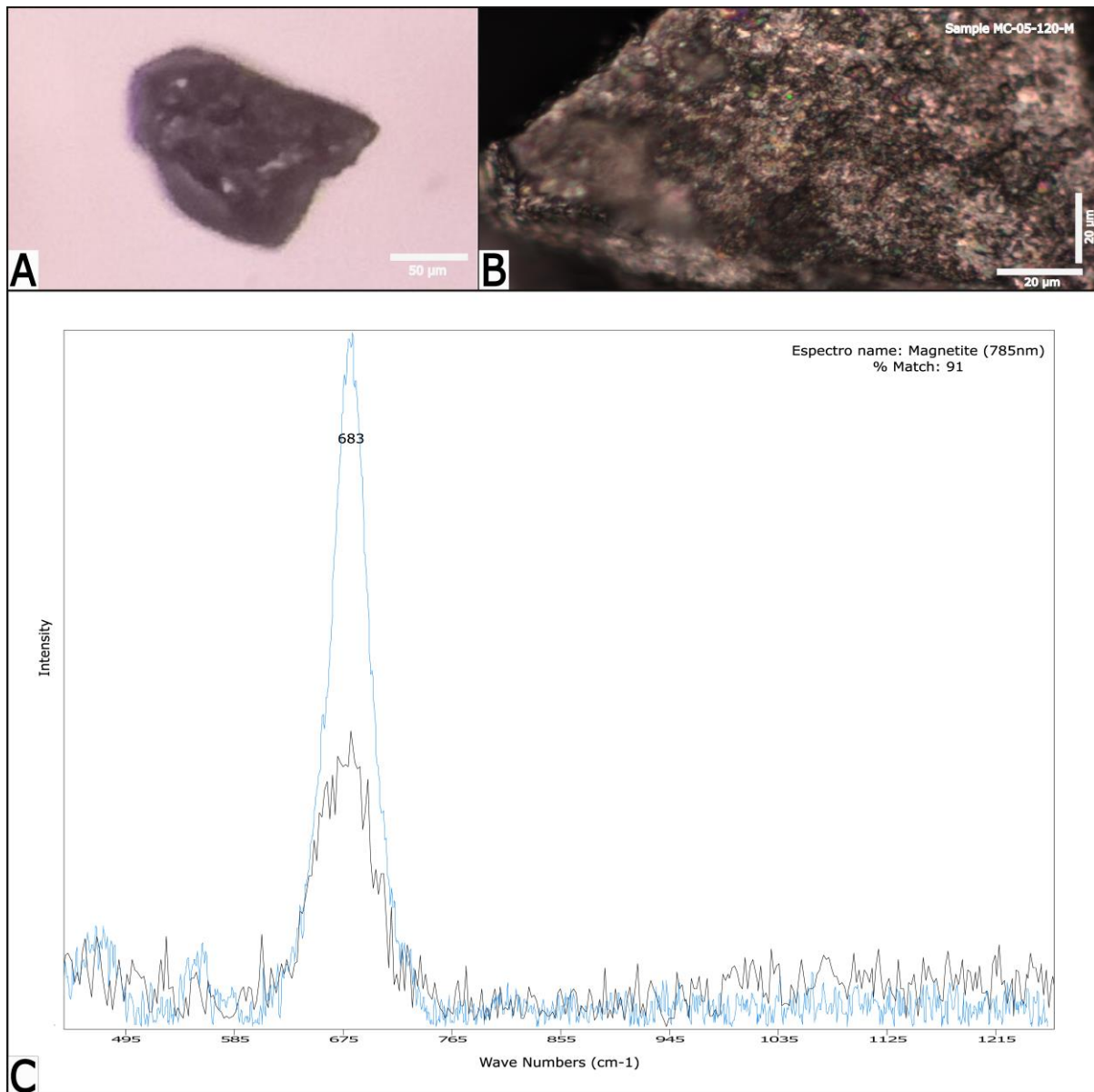
Figure 37. *A) The mineral grain whit physic characteristics of magnetite. B) Raman photo. C) Spectra Raman. Experimental spectrum (blue), RRUFF database spectrum of magnetite (black). They show an 82% of match in the range from 450 to 1257 cm^{-1}, and have a characteristic peak at approximately 683 cm^{-1}.*

Five satisfactory experimental spectra were obtained that show a high similarity with the *hematite* from the RRUFF database spectra. For example, the mineral grain (Figure 38A), Raman photo (Figure 38B), and experimental (blue) and RRUFF database hematite spectrum (black) (Figure 38C) are shown in Figure 38. The experimental spectrum shows 85% agreement with the RRUFF database spectrum of hematite. The coincidence intervals are between approximately 200 and 1150 cm^{-1}, and the most representative peaks are found at 230, 248, 292, 410, 500, and 610 cm^{-1}.
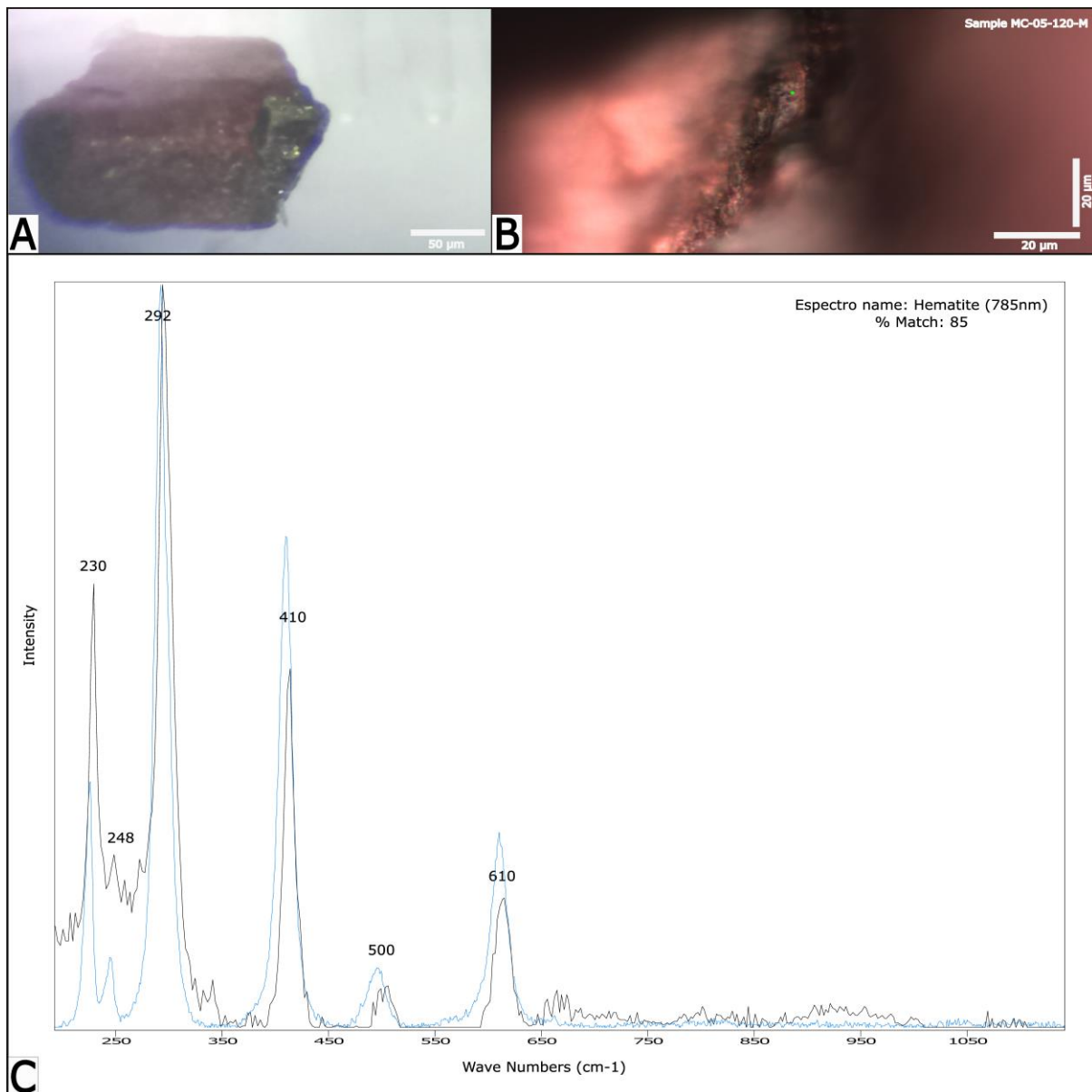
Figure 38. *A) The mineral grain whit physic characteristics of hematite. B) Raman photo. C) Spectra Raman. The experimental spectrum (blue) shows 85% agreement with the RRUFF database spectrum (black) of hematite with representative peaks at 230, 248, 292, 410, 500, and 610 cm^{-1}.*

4.8 Chemical analysis by X-ray photoelectron spectroscopy (XPS)

This XPS analysis has identified three different spectra for each analyzed fraction: magnetic, low-magnetic, and non-magnetic. These are differentiated by the atomic percentage of chemical elements contained in each mineral, which makes each spectrum show characteristic peaks: these elements present similarities in composition to iron oxide, amphibole, and plagioclase. It is possible to confirm this information with a more exhaustive analysis of the data obtained; however, in this case, the analysis was carried out to identify REEs.

The spectrum in Figure 39 was obtained from the non-magnetic fraction of sample MC-17-120-N. The spectrum allows recognition of the composition of the analyzed material using the atomic percentage of chemical elements present in the sample. In this case, O, C, Si, Mg, Al, Ca, and Na are identified, with 58.7, 14.7, 13.3, 4.9, 4.4, 2.3, and 1.8 atomic percentages respectively. The chemical elements in the sample similarities to plagioclase. The dominant peaks correspond to O at approximately 540 eV, C at 290 eV, and Si at approximately 100, 130 eV. So are the less dominant peaks: Mg, Al, Ca, and Na. Mg with three representative peaks at approximately 80, 95, and 320 eV. Al with two characteristic peaks at approximately 90 and 120 eV. Ca shows two peaks at approximately 360 and 420. Finally, Na shows two peaks at approximately 490 and 1090 eV.
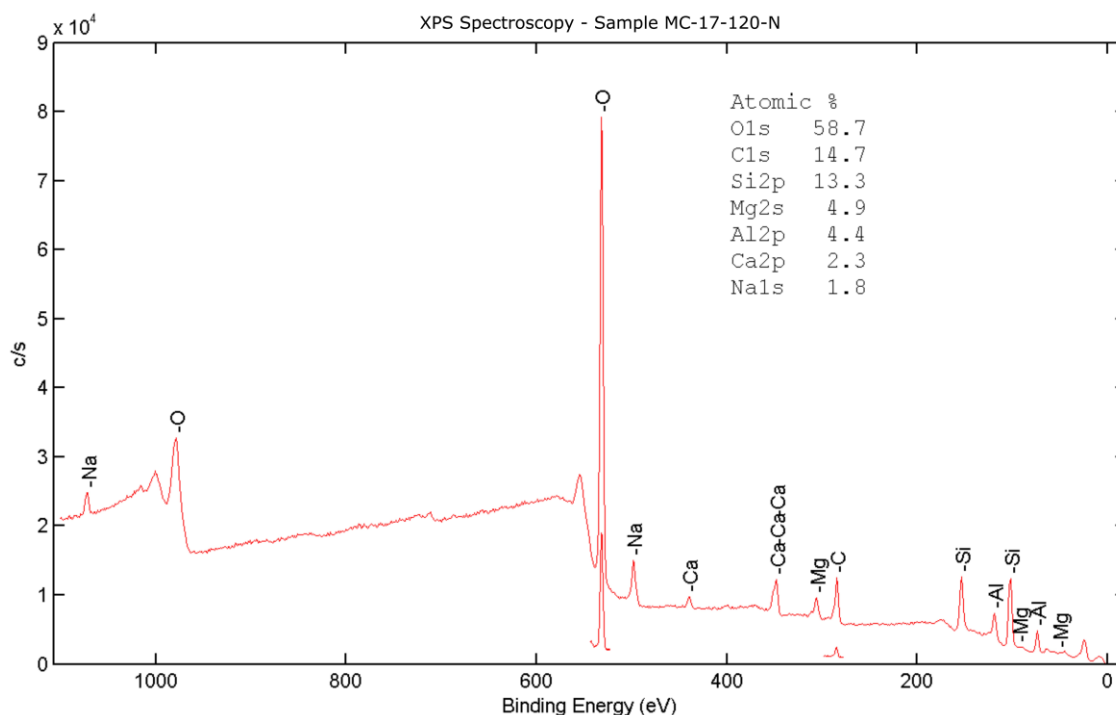
Figure 39. *Spectrum obtained from the XPS analysis of the magnetic fraction of the MC-17 sample. The spectrum shows the presence of seven elements, O, C, Si, Mg, Al, Ca, and Na. The dominant peaks correspond to O at approximately 540 eV, C at 290 eV and Si at approximately 100, 130 eV. So are the less dominant peaks Mg, Al, Ca, and Na. Mg with 3 representative peaks at approximately 80, 95 and 320 eV. Al with 2 characteristic peaks at approximately 90 and 120 eV. Ca shows 2 peaks at approximately 360 and 420. Finally, Na shows 2 peaks at approximately 490 and 1090 eV.*

Figure 40 shows the results of the atomic percentage of each element identified in the sample and represented in a spectrum of sample MC-05-120-L. Similar results of the elements were found in samples MC-12-120-M and MC-17-120-M. The elements identified are O, C, Si, Ca, Al, Na, Fe, and Mg. They present atomic percentages of 64.6, 14.7, 14.2, 3.9, 1.3, 0.9, 0.5, <.1, respectively. The chemical elements allowed find similarities with the chemical composition of an amphibole. The peaks of the three elements with the highest percentage, O, C, and Si, are distributed throughout the spectrum. O is found at approximately 550 eV and 980 eV, the C at approximately 180 eV, followed by Si at approximately 100, 130 eV. In this spectrum, the peak representing Mg stands out; this peak has a highly pronounced peak in the 320 eV range and two smaller peaks at approximately 80 and 95 eV. On the other hand, the peaks representing Ca, Al, Na, and Fe have little pronunciation. Ca shows two peaks at approximately 360 and 420 eV. Al with two characteristic peaks at approximately 90 and 120 eV. Na shows two peaks at approximately 490 and 1090 eV. Finally, the peaks and Fe are shown at 50, 700, and 800 eV.
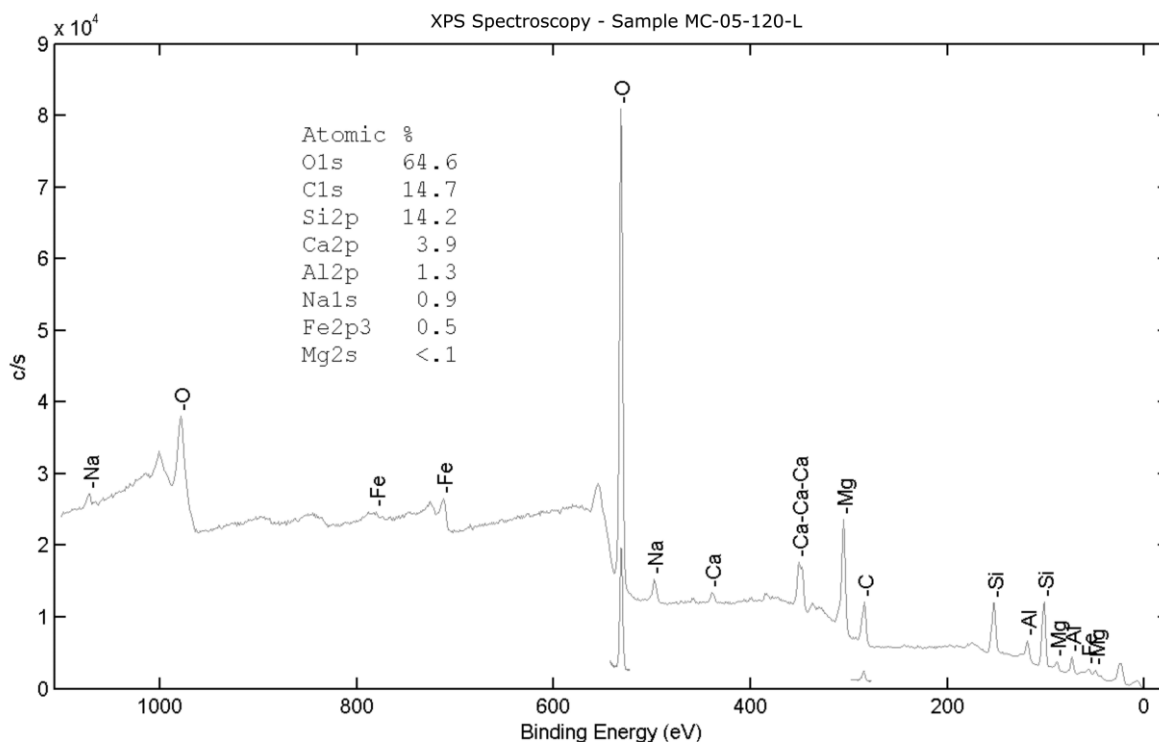
Figure 40. *Spectrum obtained from the XPS analysis of the magnetic fraction of the MC-05 sample. The spectrum shows the peaks of elements presents in the sample analyzed. In this spectrum the peak representing Mg stands out, this peak has a high pronounced peak in the 320 eV range and two smaller peaks at approximately 80 and 95 eV. Also, O is found in at approximately 550 eV and 980 eV, the C at approximately 180 eV, followed by Si at approximately 100, 130 eV. On the other hand, the peaks representing Ca, Al, Na and Fe have little pronunciation. Ca shows 2 peaks at approximately 360 and 420 eV. Al with 2 characteristic peaks at approximately 90 and 120 eV. Na shows 2 peaks at approximately 490 and 1090 eV. Finally, the peaks and Fe are show of 50, 700 and 800 eV.*

The spectrum in Figure 41 was obtained from the XPS analysis of the fraction MC-12-120-M and allows us to recognize different chemical elements: O, C, Si, Fe, Al, Mg, Ca, N, Ti, and Na, ordered from highest to lowest atomic percentage. The same elements were found in samples MC-05-120-M and MC-17-120-M. The chemical elements present in the sample indicate similarities in the composition of iron oxides, such as magnetite or hematite, minerals found in previous analyses, however, it could be a titanomagnetite or ilmenite since it presents a small amount of Ti. The distinctive feature of this spectrum is the Fe peaks between the values of 50, 700, and 800 eV. However, the dominant peaks correspond to O at approximately 550 eV and 980 eV, followed by C at about 180 eV. So are the less dominant peaks Si, Fe, Al, and Mg. The peaks of these elements lie within the approximate range of 10 to 580 eV. Some Ca, N, and Ti peaks are also found within this range. However, Na is found at 490 and 1050 eV. Minerals occur with lower atomic percentages.
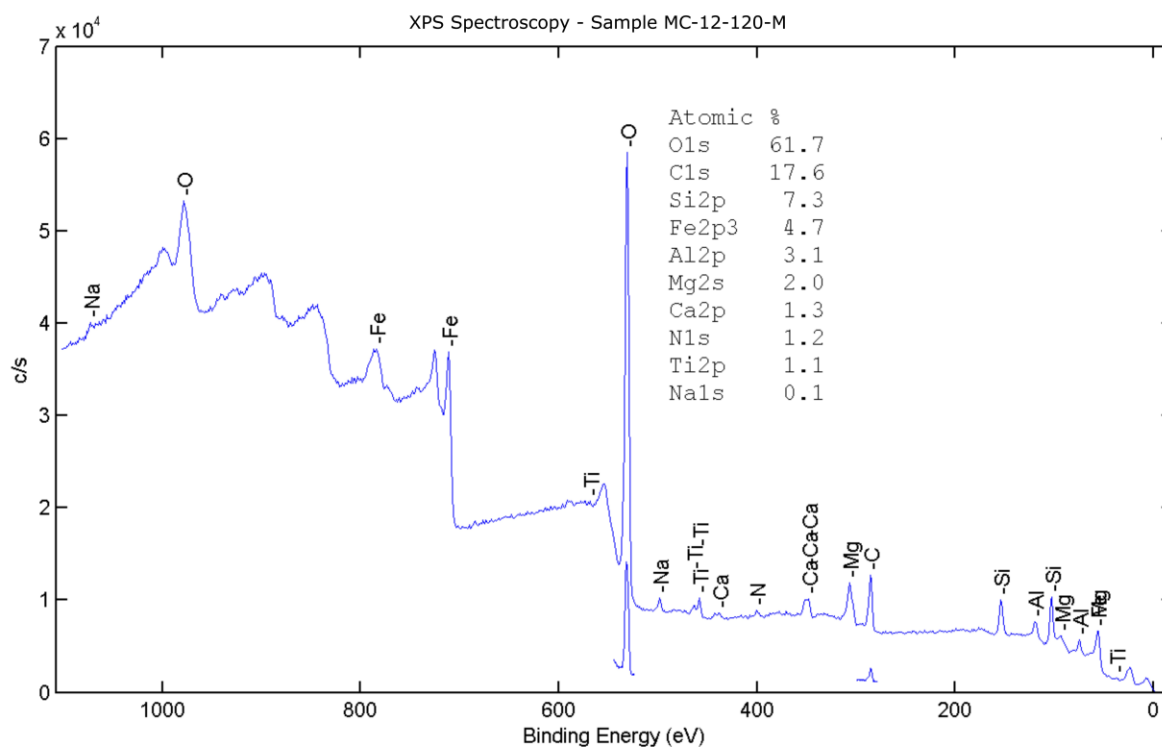
Figure 41. *Spectrum obtained from the XPS analysis of the magnetic fraction of the MC-12 sample. The figure shows the peaks and atomic percentage of different elements. The predominant elements are O, C, Si, and Fe. The dominant peaks correspond to O at approximately 550 eV and 980 eV, followed by C at approximately 180 eV. Thus, other the distinctive peaks of Fe in approximately the values of 50, 700 and 800 eV. After the above elements are Si, Fe, Al, and Mg, the peaks of these elements are found in the approximate range of 10 to 580 eV. Finally, some peaks of Ca, N and Ti are also in this range. However, Na is found at 490 and 1050 eV.*

The atomic percentage of elements of the three samples is shown in Table 8. The table indicates that oxygen is the most abundant element across all samples; its atomic percentage varied between 58.7 and 64.6. The second predominant element is carbon, with percentages higher than 14 but lower than 18. Silicon is found in percentages between 7.3 and 14.2. Iron is also found with an atomic percentage of 4.7 in the magnetic sample and a null and almost null percentage in the magnetic and low magnetic samples, respectively. Aluminum, magnesium, and calcium are found in percentages between 1.3 and 4.9, except for the almost null presence of magnesium in the low magnetic sample. Nitrogen, titanium, and sodium are found in percentages lower than 1.8 or null. None of those mentioned above elements belong to the REEs.

Table 8. *Atomic percentage of elements of samples; MC-12-120-M, MC-05-120-L, and MC-17-120-N, according XPS analysis.*

Atomic percentage of elements		
Sample	MC-12-120-M	MC-05-120-L	MC-17-120-N
Element	Atomic Percentage (%)		
O1s	61.7	64.6	58.7

C1s	17.6	14.7	14.7
Si2p	7.3	14.2	13.3
Fe2p3	4.7	0.5	0
Al2p	3.1	1.3	4.4
Mg2s	2	<0.1	4.9
Ca2p	1.3	3.9	2.3
N1s	1.2	0	0
Ti2p	1.1	0	0
Na1s	0.1	0.9	1.8

CHAPTER 5: DISCUSSION

5.1 Morphometric analysis of lithics fragments and sand-sized particles associated to CCVC.

Most sand-sized and lithic fragments from the river systems connected to CCVC had low sphericity and angular or subangular forms. In this context, the shape impacts particle flow through the water stream (Basile, 2018). Particles with less spherical forms have lesser mobility during bottom transport than spherical particles (Pettijohn, 1970, as cited in Basile, 2018). However, other factors influence the shape of the particles, including their density, size, or even the river inflow, size, or order. In this case, the particles of the samples were taken from the first and second order rivers and were no more than 15 km from the river course headwaters, negating any significant movement.

5.2 The mineralogical association of the sands associated to CCVC as determined by analytical techniques

Table 9. Minerals identified in the different fractions obtained from magnetic separation.

Minerals identified in the different fractions	Non-magnetic fraction	Low-magnetic fraction		Magnetic fraction
	Feldspars-Plagioclase	Amphibole	Pyroxenes	Iron Oxides
	Andesine	Hornblende (Magnesio-hastingsite)	Augite	Magnetite
	Labradorite		Enstatite	Hematite

Due to past volcanic activities, the study area hosts pyroclastic deposits, which have been eroded by the action of water from tributaries in the area to form associated minerals that may reveal important details about past geological events. Several mechanisms were involved in creating these magmatic igneous rock-forming minerals related to the volcanism of the area. Among these is the process of magma crystallization, which allows one to comprehend and distinguish between different minerals and rocks. The crystallization process of minerals has been represented in a diagram designated Bowen's reaction series (Figure 42), which refers to the formation of different minerals concerning the cooling of the magma.
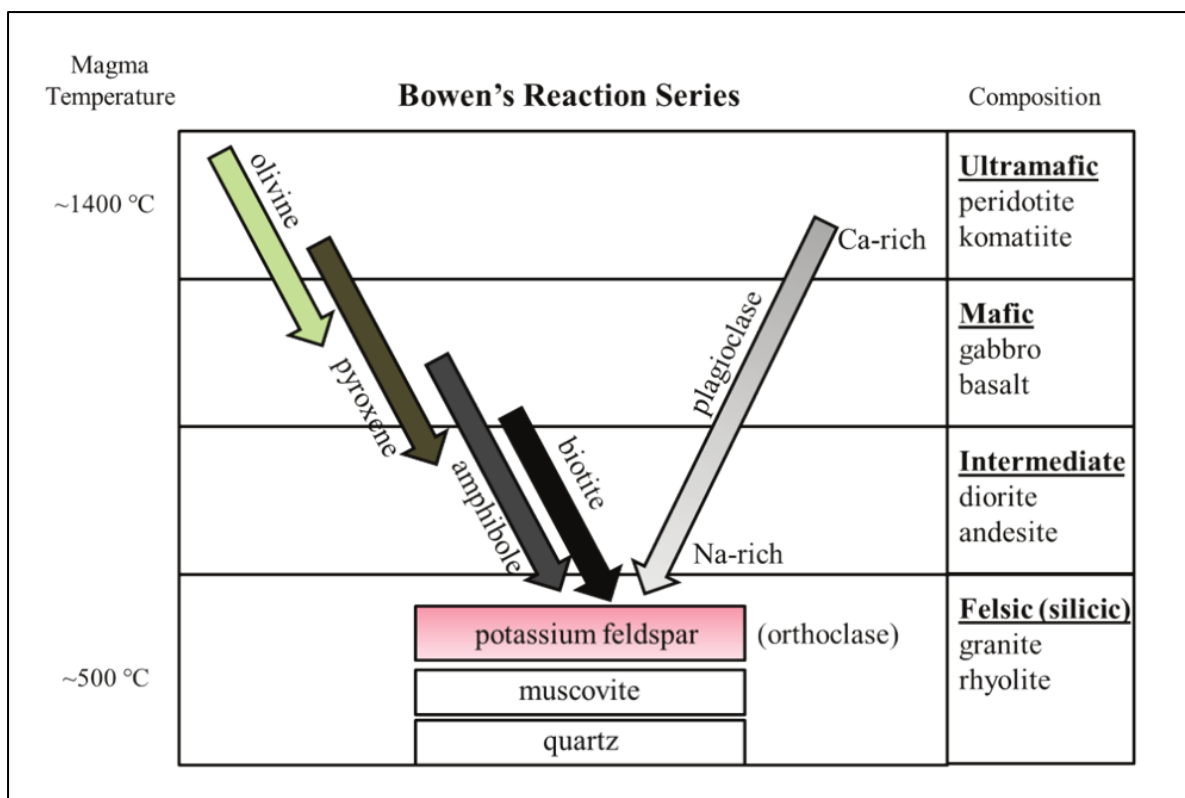
Figure 42. Bowen's Reaction Series Bowen. Mineral crystallization sequence following magma cooling (Modified from Deline et al., 2015)

The two plagioclases (andesine and labradorite) recognized in the non-magnetic fraction are difficult to distinguish by stereomicroscopic observation of their similar characteristics. However, XRD analysis made it possible to identify them, but with a significant similarity between the spectra of these two plagioclases. Probably because they belong to the plagioclase group and have a similar chemical composition; moreover, using Raman analysis, it was possible to distinguish a large number of spectra identical to that of labradorite and very few to the spectrum of andesine. The various plagioclases and their mineralogical association are related to their formation process.

The order in which the minerals crystallize in magma as the temperature drops determines the mineral associations and proportions that make up felsic and mafic igneous rocks (Varela, 2014). Plagioclases can crystallize at both high and low temperatures; however, their composition varies concerning their crystallization temperature. Bowen's reaction series shows that labradorite crystallizes faster than andesine at higher temperatures. However, these two minerals crystallize before oligoclase and after bytownite and anorthite, so labradorite and andesine are typical of mafic and basic rocks, respectively. Minerals that form at high temperatures of ~1800°C or slightly less are typically found in ultramafic rocks, and as the temperature decreases, minerals typical of mafic rocks are formed; intermediate rocks are

created by minerals that crystallize at temperatures between ~600°C and ~900°C; felsic rocks are formed at temperatures lower than this (Figure 42) (Álvarez & Córdoba, 2021).

Labradorite is typically found in mafic igneous rocks and is associated mainly with pyroxenes, amphiboles, and magnetite. At the same time, andesine is widespread in igneous rocks with an intermediate silica content and is associated with biotite, hornblende, quartz, potassic feldspar, and magnetite (John et al., 2003). Therefore, plagioclase is significant in basic to intermediate volcanic rocks such as basalts and andesites (González, 2015).

Plagioclase has also been identified in the work of Rengel, 2020. In the analysis of pyroclastic current from Cuicocha, she identified the presence of translucid crystals corresponding to plagioclase. In this context, similar results have been found in the research conducted by Sánchez (2017), which focused on a mineralogical and multi-elemental analysis of the volcanic ash, a product of the Cotopaxi eruption of 2015. Through XRD analysis, the researchers determined that one of the majorities of the minerals present in the crystallin phases analyzed are plagioclase minerals.

Pyroxenes, including enstatite and augite, and amphiboles, including magnesio-hastingsite of the hornblendes group, could be distinguished in the low-magnetic section. According to the stereomicroscopic observations of fraction collected to 120 mesh, the percentage abundance of amphiboles is 20% higher than that of pyroxenes. However, by XRD analysis, it was impossible to identify pyroxenes, probably because their concentration in the fraction analyzed was too low to be detected by the equipment. By Raman analysis, it was possible to identify the presence of amphiboles and two types of pyroxenes.

Pyroxenes are one of the main minerals that comprise igneous rocks. Pyroxenes, like plagioclase, crystallize as a function of magma cooling, so they crystallize under certain temperature conditions. The minerals composed of iron, magnesium, silicon, and oxygen are evident at temperatures of about ~1800 ℃. As the temperature drops, pyroxene stabilizes, and calcium starts to show up in the minerals formed at about ~1100 ℃ (Figure 42), and amphiboles appear when the temperature drops to about ~900 ℃ (Figure 42) (Álvarez & Córdoba, 2021).

Pyroxenes were identified, including augite and enstatite. In igneous rocks, augite is the most common pyroxene, whereas hornblende is the most frequently amphibole (Varela, 2014). Augite usually occurs in basalts and mafic igneous rocks. It is also frequently found in ultramafic rocks and is associated with orthoclase, labradorite, olivine, and amphiboles, while enstatite is associated with olivine, pyrope, clinopyroxene, phlogopite, and diopside (John et

al., 2003). Thus, pyroxene forms a significant group of minerals in igneous rocks. In addition, the magnesio-hastingsite of the hornblende group is primarily found in alkaline basalts, latites, andesites, carbonatites, and tuffs and exhibits associations with olivine, plagioclase, and pyroxenes (John et al., 2003). Hornblende has also been identified in the pyroclastic current form CCVC of the work of Rengel, 2020.

Magnetite and hematite were identified in the magnetic fraction. Magnetite is produced in various geological environments and is one of the more common iron oxide minerals (Sánchez, 2017). Magnetite is a typical accessory mineral found in igneous rocks. In this context, magnetite is associated with silicate, rutile, apatite, ilmenite, and chromite pyroxenes (John et al., 2003). Stereomicroscopic observations, XRD, and Raman analysis have recognized magnetite. However, hematite has been identified in stereomicroscopic observation and Raman analysis. Hematite commonly occurs as an accessory mineral in igneous rocks and, in the igneous context, is associated with ilmenite, rutile, and magnetite (John et al., 2003). In this context, the iron oxides, magnetite, and hematite have also been identified in the mineralogical and multi-elemental analysis of the volcanic ash, a product of the Cotopaxi eruption in 2015, by Sánchez (2017).

The presence of this mineral association in the fluvial sands indicates the erosion and transport of pyroclastic material by the radial fluvial system. Also, it shows that these materials were formed from magmas of mafic and intermediate composition that ascended to the earth's surface and solidified during volcanic activity, creating various volcanic rocks, such as andesites, dacites, and rhyolites.

5.3 Fraction where the highest concentration of industrially valuable minerals and their potential uses and applications for the more representative minerals found.

The fraction was collected in 120 mesh containing 92.2% mineral and 7.8% lithic particles. Therefore, most of the minerals of interest are between 0.25 and 0.125 mm in diameter. In this fraction, it was possible to identify several heavy minerals, most of which have industrial and economic potential. Magnetite, hematite, amphibole, and pyroxene are some of the heavy minerals identified in the sand samples.

The demand for these minerals is rising daily due to their usage in numerous high-tech applications, such as electronics, solar cells, nuclear reactors, green technology, and nano and space technology (Subasinghe et al., 2022). Therefore, heavy minerals are the minerals with

the highest industrial value. However, not all minerals are found in large quantities in the samples analyzed. According to the magnetic separation, the magnetic fraction is the most representative, consisting of two iron oxides: magnetite and hematite. These two minerals together are found in quantities of 59.05% of the mass of all the samples of fluvial sands with the CCVC (See Table 4).

Iron oxide functions as a reducing agent on various harmful substances in aqueous solutions, which is why iron nanoparticles are employed to remove toxic waste (Mantuano et al., 2020). In Ecuador, some effluents have high levels of Cr (VI), mainly from the tanning industry, which has caused a great environmental impact; however, adsorbent agents such as magnetic nanoparticles are an alternative to eliminate this pollutant (González & Silva, 2023). Removing these types of contaminants can make a significant contribution to the environment. González & Silva (2023) investigated the creation of magnetite nanoparticles coated in chitosan for the adsorption of hexavalent chromium; in this investigation was possible produced nanoparticles with an average diameter of 31.85 nm, a maximum adsorption capacity of 294.12 mg/g at 60 °C, and the most significant adsorption percentage of 99.70%, so proving that hexavalent chromium adsorption was possible.

Additionally, several biomedical applications have shown promise for iron oxide nanoparticles. Specifically, magnetite nanoparticles are affordable, biocompatible, chemically stable, and highly saturated magnetized (Ganapathe et al., 2020). Drug delivery, chemotherapy, magnetofection, hyperthermia, organ/tissue imaging, theranostic platforms, and immunoassays are a few of the biomedical uses of magnetite nanoparticles (Ortega & Reguera, 2019). Another practical current application of ferrimagnetic materials such as magnetite is ferrofluids. Ferrofluids are a practical modern usage for ferrimagnetic minerals like magnetite. Ferrofluids have several remarkable applications, including the rotating shafts of hard drives, speakers, and loudspeakers in sound systems, which vibrate and convert electric impulses into sound waves (Mazo-Zuluaga, 2011).

Additionally, Iron oxides have been utilized in pigments and anticorrosive paints for decades. Iron oxide-based pigments are non-polluting and reasonably priced, providing a new option to the industrial sector (Restrepo et al., 2009). Magnetite-based pigments are also utilized in magnetic ink character recognition devices (Unsoy et al., 2015).

In Ecuador, there is much talk about the black sands of the coastal areas, which contain large amounts of iron oxides used mainly to produce pigments and cement aggregates. According to

Chuquirima & Cortez (2014), cement has been produced from secondary placer deposits in Manabí and Guayas and from black sands in Santa Elena that make black pigment from magnetite and white pigment from titanium dioxide.

However, for the assignment of any use or application, a more detailed analysis of the chemical composition of the minerals is necessary to approve their quality. In addition, it is essential to know the amount of material available in the area.

5.4 The existence of Rare Earth Elements

Recent market turbulence for REEs has deepened our understanding of the global resources for these elements (Gronek & Łęczycki, 2017). High-tech applications in various industries, including electrical and electronics, automotive, renewable energy, medical, and defense, use REEs (Dushyantha et al., 2020). Hence, there is interest in identifying REEs in the minerals of the fluvial sands associated with the CCVC. In this research and using the spectra obtained from the XPS analysis, it has been possible to find chemical elements common in the environment surrounding us and more unusual and valuable elements in several aspects.

The spectra of the different samples show high values of atomic percentage of oxygen and carbon. The increased oxygen values are due to the environment since we are surrounded by oxygen. The high carbon values may be due to the different contamination of the sample due to the constant manipulations in the sample preparation process. The atomic percentage of each element varies depending on the sample. The results of the analysis of the magnetic sample stand out for the values of atomic percentages in the elements of Si, Fe, Al, and Mg. In addition, the presence of Ti is likely due to the presence of titanomagnetite or ilmenite, minerals not determined in the previous analysis. However, it could be present in low quantities and, therefore, more complex to identify. Minerals holding titanium, REEs, and zirconium are essential industrial commodities worldwide (Subasinghe et al., 2022). Also, in the results of the low-magnetic sample, the atomic percentage values of the elements Si, Ca, and Al stand out; however, the elements Na, Fe, and Mg present atomic percentage values lower than 1. On the other hand, in the non-magnetic sample, Si is an outstanding element, followed by Mg, Al, Ca, and Na. However, with the spectra XPS and other methods used for mineralogical characterization, it was impossible to identify the presence of REEs.

The REEs are found in chemical compounds within the crust of the Earth; pure element deposits are not found there. (Gronek & Łęczycki, 2017). REEs deposits have been classified

into primary and secondary deposits. The primary is hydrothermal, metasomatic, and magmatic in origin (Calvo, 2010), and the mineralization that has been concentrated by weathering and sedimentary processes is found in secondary deposits (Zappettini, 2022). Primary origin deposits are linked to alkaline igneous rocks and carbonatites, which are rich in light rare earth elements (LREE), and peralkaline igneous rocks, which are generally enriched in zirconium, yttrium, and heavy rare earth elements (HREE) (Castor & Hedrick, 2006). Furthermore, from the calc-alkaline volcanic belt of the Calimani-Harghita Mountains (Rumenian Carpathians), Peccerillo & Taylor (1976) report REEs, Y, Rb, Sr, Cs, Ba, Pb, Th, U, Zr, Hf, and Sn for a basalt, low-Si andesite, andesite, high-K andesite, dacite, and rhyolite.

Other primary occurrences are linked to IOCG (Iron Oxide-Copper-Gold) types of deposits (Bohórquez et al., 2013). In this IOCG system, the primary sources of REEs in magnetite-dominated ores are rock-forming minerals such as titanite, apatite, and epidote-allanite, and REEs that are found in apatite in hematite-rich associations; these include silicates (allanita, stillwellita), carbonates (bastnasite, synchysite), and phosphates (monazite, xenotime, britolite) (Zappettini, 2022). Conversely, one of the deposit's secondary ones originates from the transport of moved colluvial, alluvial, and marine placers (Calvo, 2010).

Xenotime and monazite, the ore minerals, support transport from their formation environment to the depositional sites due to their weight and chemical stability, generally concentrated on marine coasts and river banks (Zappettini, 2022). Furthermore, extracting heavy minerals like rutile, zircon, and ilmenite typically results in the recovery of monazite and xenotime as a by-product. These deposits are a source of LREE and thorium (Th) (Araya et al., 2016). The easy recovery of REEs minerals from placer deposits has made them attractive, but because of the issues surrounding the environmental management of radioactive waste like Th and U, placer deposit development has been limited (Zappettini, 2022).

Due to their scarcity and diversity, rare earth element deposits are challenging to classify; some deposit types have only one known example, while other deposits have processes that overlap and fall into more than one category (Araya et al., 2016). Therefore, because one of the sources for obtaining REEs is deposits of magmatic origin, the possibility of the existence of these elements within the fluvial sands of the CCVC has been seen. The minerals composing the fluvial sands of CCVC originating from pyroclastic deposits tend to contain rare earth elements since they come from fragments of magmatic origin. The minerals commonly containing this type of elements are monazite, apatite, and xenotime; these minerals can also be present as

inclusions of other minerals, in which it is common to identify traces of REEs. An example is found in the investigation of coastal black sand samples collected from the Northern part of Kos by Eliopoulos & Economou-Eliopoulos (2019). This investigation revealed the presence of abundant Ti-magnetite and magnetite with the inclusion of apatite (more than 220 ppm ΣREEs) and monazite with a varying composition [(Ce, La, Th, Nd, Y) PO_4 and (Ce, La, Nd, Pr, Sm) PO_4]. A volcanic source can be connected to magnetite separates from these black coastal sands (Tzifas et al., 2017). Additionally, in the investigation by Yang et al., 2002 which shows compositional fractions of REEs contributed by minerals in the Changjiang and Huanghe sediments, traces of rare earth elements have also been recorded in feldspars and hornblendes, minerals identified in the samples of this investigation. Therefore, the possibility of the existence of REEs, possibly in relatively small quantities, which makes their identification by XPS analysis difficult, cannot be ruled out.

CHAPTER 6: CONCLUSIONS AND FUTURE WORKS

6.1 Conclusions

The lithic fragments and sand-sized particles are primarily found in angular and subangular shapes, which indicates that they have been transported over relatively short distances.

The fluvial sand samples associated with the CCVC present a mineralogical composition mainly composed of iron oxides at 59.05%, plagioclase at 27.55%, pyroxenes, and amphibole at 13.40%. Plagioclase comes in the forms of labradorite and andesine. Pyroxenes include enstatite and augite; hornblende is the mineral found in amphibole. Included in iron oxides are magnetite and hematite. This mineral association suggests that these minerals originated from the solidification of mafic and intermediate magma during volcanic activity.

The grain sizes of the minerals of interest are found in the fraction retained in the 120 mesh. Therefore, they are presented in 0.25 to 0.125 mm in diameter ranges. In this fraction, minerals account for 92.1% of the total mass, with lithic particles making up the remaining 7.9%. This fraction that separated according to its degree of magnetism shows great abundance in the magnetic fraction with 59.05% of the mass in all the samples. Consequently, the most representative fraction is the magnetic fraction, composed of magnetite and hematite, minerals of great industrial value.

The most representative minerals, magnetite and hematite, could be used in the remove of toxic waste, biomedical applications and ferrofluids. These minerals could also be utilized to make pigments and paints due to their anticorrosive properties. However, it is necessary to conduct a quality study of these minerals, evaluate the resources, and quantify the reserves.

Employing the XPS (0.01% sensitivity), the analysis focused on identifying REEs; it was impossible to locate them. However, they may be in deficient concentrations, and their study may require more sensitive analytical techniques.

6.2 Future works

Future work could continue with research focused on the magnetic fraction, which is often the source of REEs. A new methodology focused exhaustively on identifying these REEs could be used to rule out their existence or identify any of them. Inductively Coupled Plasma Atomic Emission Spectroscopy (ICP-OES), or Inductively Coupled Plasma Mass Spectrometry (ICP-MS) would be good options for the identification or rule out the presence of these elements.

REFERENCES

Almeida, M. (2016). *Estudio Petrográfico y Geoquímico del Volcán Cotacachi – Provincia de Imbabura. Ecuador* [Undergraduate thesis, Escuela Politécnica Nacional].

Álvarez Contreras, D. G. B., & Córdoba, A. L. (2021). Tabla periódica de los elementos asociada a geología. *Revista Iberoamericana de Tecnología en Educación y Educación en Tecnología*, (29), 79-85.

Augusto, J. (2019). *Seismic interferometry for Andean volcanoes: Characterization and monitoring of the subsurface* [Doctoral thesis, Universidad Nacional de La Plata].

Balaram, V. (2019). Rare earth elements: A review of applications, occurrence, exploration, analysis, recycling, and environmental impact. *Geoscience Frontiers*, *10*(4), 1285-1303. https://doi.org/10.1016/j.gsf.2018.12.005

Barragan, R., Geist, D., Hall, M., Larson, P., & Kurz, M. (1998). Subduction controls on the compositions of lavas from the Ecuadorian Andes. *Earth and Planetary Science Letters*, *154*, 153–166. https://doi.org/10.1016/S0012-821X(97)00141-6

Basile, P. A. (2018). Transporte de sedimentos y morfodinámica de ríos aluviales. *Biomass Chem Eng*.

Bernard, B., & Andrade, D. (2011). Volcanes Cuaternarios del Ecuador Continental. Quito, Ecuador IG – EPN/IRD, *Informative poster.*

Bohorquez, J., Jara, R., Mamani, Y., Guerrero, L., & Villafranca, A. (2013). Ocurrencias de Tierras Raras en el Perú. *Boletín de la Sociedad Geológica del Perú*, *107*, 146-150.

Boland, M. P., Ibandango, C., McCourt, W., Aspden, J., Hughes, R., & Beate, B. (2000). Geology of the Western Cordillera between 0-1 N, Proyecto de Desarrollo Minero y Control Ambiental, Programa de Informacion cartografica y Geológica. *CODIGEM-BGS, Quito, Ecuador.*

Bunaciu, A., UdriŞTioiu, G., & Aboul, Y., (2015). X-ray diffraction: instrumentation and applications. *Critical reviews in analytical chemistry*, *45*(4), 289-299.

Caisachana, M. (2021). *Design and synthesis of surface-enhanced Raman scattering active surfaces* [Undergraduate thesis, Universidad de Investigación de Tecnología Experimental Yachay].

Calderón Allauca, Á. I. (2013). *Caracterización mineralógica y morfométrica de los sedimentos eólicos de la Península de Paracas-Ica y su relación con las variables meteorológicas durante el invierno* [Undergraduate thesis, Universidad Nacional Mayor De San Marcos].

Calvo, G. 2010. Aspectos geoquímicos y metalogenéticos de las tierras raras. Resúmenes extendidos, XV Congreso Peruano de Geología, Cusco, p. 388–391.

Carrión-Mero, P., Duenas-Tovar, J., Jaya-Montalvo, M., Berrezueta, E., & Jiménez-Orellana, N. (2022). Geodiversity assessment to regional scale: Ecuador as a case study. *Environmental Science & Policy*, *136*, 167-186.

Castor, S. B., & Hedrick, J. B. (2006). Rare earth elements. *Industrial minerals and rocks*, *7*, 769-792.

Cerquera, A., Rodríguez, A., & Ruano, F., (2017). *Análisis mineralógico, químico y porosimétrico de los agregados pétreos de una cantera perteneciente a la formación geológica de la sabána en el municipio de Soacha – Cundinamarca* [Undergraduate thesis, Universidad Católica de Colombia].

Chastain, J., & King Jr, R. C. (1992). Handbook of X-ray photoelectron spectroscopy. *Perkin-Elmer Corporation, 40,* 221.

Chuquirima, M., & Cortez, L. (2014). E*studio y obtención de material de hierro a partir de arenas ferruginosas* [Undergraduate thesis, Escuela Politécnica Universidad Nacional].

De la Hoz, Gonzalo (2012). Las tierras raras: elementos claves del siglo XXI. *Temas de Biologia y Geologia del NOA,* 2(2), 39-47.

Deline, B., Harris, R., & Tefend, K. (2015). *Laboratory manual for introductory geology*. University System of Georgia, University Press of North Georgia.

Dushyantha, N., Batapola, N., Ilankoon, I. M. S. K., Rohitha, S., Premasiri, R., Abeysinghe, B., ... & Dissanayake, K. (2020). The story of rare earth elements (REEs): Occurrences,

global distribution, genesis, geology, mineralogy and global production. *Ore Geology Reviews*, *122*. https://doi.org/10.1016/j.oregeorev.2020.103521

Eliopoulos, D. G., & Economou-Eliopoulos, M. (2019). Trace element distribution in magnetite separates of varying origin: Genetic and exploration significance. *Minerals*, *9*(12), 759.

Galán, C., Martin, C. V., & Molia, M. (2009). Análisis por espectrocopía Raman y XPS de muestras de Paramoudras en areniscas de la Formación Jaizkibel. Pag. Web aranzadi-sciences. Org, Archivo PDF.

Ganapathe, L. S., Mohamed, M. A., Mohamad Yunus, R., & Berhanuddin, D. D. (2020). Magnetite (Fe3O4) nanoparticles in biomedical application: From synthesis to surface functionalisation. *Magnetochemistry*, *6*(4), 68.

García, E. (2020). *Petrological study of the Cotacachi-Cuicocha Volcanic Complex, Ecuador: Understanding the eruptive dynamic and evolution of the magma* [Undergraduate thesis, Universidad de Investigación de Tecnología Experimental Yachay].

González, M., & Silva, J. (2023). Síntesis de nanopartículas de magnetita recubiertas de quitosano para la adsorción de cromo hexavalente. *Perfiles*, *1*(29), 78-89.

González, P.D. 2015. Textura de los cuerpos ígneos. En: Llambías, E.J. (ed.), *Geología de los cuerpos ígneos, Asociación Geológica Argentina* (167-195), Buenos Aires

Gronek, S., & Łęczycki, K. (2017). Rare earth elements and their importance for economy and safety. *Prace Naukowe Instytutu Technicznego Wojsk Lotniczych*, *40*(2), 129.

Gutierrez, R. R. G., & Rondon, M. C. F. (2018). Funcionamiento del aparato de laboratorio SBAN en una Universidad Venezolana para el secado de arena. *Scientia et technica,* 23(1), 68-75.

Hall, M. L., Samaniego, P., Le Pennec, J. L., & Johnson, J. B. (2008). Ecuadorian Andes volcanism: A review of Late Pliocene to present activity. *Journal of Volcanology and Geothermal Research*, *176*(1), 1–6. https://doi.org/10.1016/j.jvolgeores.2008.06.012

Jácome, G., Mejía, J., Guerra, N., Romero, A., Puedmag, V., Padilla, C., Tanaí, I., & Pupiales, N. (2020). *Los volcanes de Imbabura y su tiempo geológico*. Imbabura-Ecuador. FICAYA Emprende.

John W. Anthony, Richard A. Bideaux, Kenneth W. Bladh, & Monte C. Nichols, (2003), *Handbook of Mineralogy,* Mineralogical Society of America. http://www.handbookofmineralogy.org/

Jones, G. (2009). Mineral sands: An overview of the industry. *Unpublished. Capel: Iluka Resources Limited*.

Kerguelen, J. (2016). *Caracterización y Aprovechamiento de Recursos Minerales en Colas de Terrazas Aluviales del Distrito Bagre-Nechí* [Undergraduate thesis, Universidad Nacional de Colombia].

Khan, H., Yerramilli, A. S., D'Oliveira, A., Alford, T. L., Boffito, D. C., & Patience, G. S. (2020). Experimental methods in chemical engineering: X-ray diffraction spectroscopy— XRD. *The Canadian journal of chemical engineering*, *98*(6), 1255-1266.

König, U., & Verryn, S. M. (2021). Heavy Mineral Sands Mining and Downstream Processing: Value of Mineralogical Monitoring Using XRD. *Minerals, 11*(11), 1253.

Londoño Escobar, J. I., Mojica Buitrago, J., Molano Mendoza, J. C., Cañón Romero, Y., Mosquera, G. S., Ruiz Solano, V., Pérez, N., Gutiérrez, H. M., González, M. del C., Concha, H., Galindo, B., Londoño Madrigal, S. E., & Buriticá, J. J. (Eds.). (2010). *Técnicas mineralógicas, químicas y metalúrgicas para la caracterización de menas auríferas.* Libros del Servicio Geológico Colombiano. https://doi.org/10.32685/9789589789667

Mantuano, M. O. M., Jiménez, K. X. B., Fiallo, S. F. A., Rosado, Á. R. H., & Robles, D. V. A. (2020). Biosíntesis de nanopartículas de hierro (FE_3O_4) en la remediación de aguas contaminadas. *Universidad Ciencia y Tecnología*, *24*(96), 35-45.

Márquez Medina, A. D., & Jiménez Hernández, A. (2017). Prospección de Tierras Raras ¿Una alternativa de los minerales estratégicos en México? *Geomimet*, *44*(328), 29-36.

Mazo-Zuluaga, J. (2011). Una mirada al estudio y las aplicaciones tecnológicas y biomédicas de la magnetita. *Revista EIA,* (16), 207-223.

Mendoza, A. M. A., Serrano, C. C., Gutiérrez, O. J. G., & Garzón, C. G. (2023). Análisis Sedimentológico y Estratigráfico del Estuario del Río Bunche, Provincia de Esmeraldas–Ecuador. *Revista Científica GeoLatitud*, *6*(2), 18-29.

Ochoa, L. (2022). *Estudio de recuperabilidad y calidad de minerales de tierras raras como subproducto de la minería aluvial de oro* [Master´s thesis, Universidad Nacional de Colombia].

Ortega, G., & Reguera, E. (2019). Biomedical applications of magnetite nanoparticles. In *Materials for Biomedical Engineering* (pp. 397-434). Elsevier.

Padrón, E., Hernández, P. A., Toulkeridis, T., Pérez, N. M., Marrero, R., Melián, G., Virgili, G., & Notsu, K. (2008). Diffuse CO_2 emission rate from Pululahua and the lake-filled Cuicocha calderas, Ecuador. *Journal of Volcanology and Geothermal Research*, *176*(1), 163–169. https://doi.org/10.1016/j.jvolgeores.2007.11.023

Peccerillo, A., & Taylor, S. R. (1976). Rare earth elements in East Carpathian volcanic rocks. Earth and Planetary Science Letters, 32(2), 121-126.

Pérez, M. (2019). *El comportamiento geoquímico de las Tierras raras en las aguas ácidas del sitema volcánico-hidrotermal del Puracé (Colombia)* [Master´s thesis, Centro de Investigación Científica y de Educación Superior de Ensenada].

Pidgen, A. (2014). *Cuicocha Volcano, Ecuador: reconstruction of major explosive phases through investigation of associated pyroclastic deposits* [Master's thesis, University of Oxford].

Rengel, P. (2020). *Caracterización de Depósitos de Corriente de Densidad Piroclásticas Asociados a la Cardera de Cuicocha, Norte de los Andes Ecuatorianos* [Undergraduate thesis, Universidad de Investigación de Tecnología Experimental Yachay].

Restrepo, O. J., Forero, A., & Díaz, S. (2009). Obtención de un pigmento natural para la formulación de pinturas anticorrosivas. Suplemento de la Revista Latinoamericana de Metalurgia y Materiales, S1 (1): 159-162

Sánchez Carrillo, E. P. (2017). *Análisis mineralógico y multielemental de la ceniza volcánica, colectada en una hacienda en el sector de Machachi, por difracción de rayos X (XRD) y espectrometría de masas con plasma acoplado inductivamente (ICP-MS), y sus posibles aplicaciones e impactos* [Bachelor's thesis, Pontificia Universidad Católica del Ecuador].

Sierra, D., Hidalgo, S., Almeida, M., Vigide, N., Lamberti, M. C., Proaño, A., & Narváez, D. F. (2021). Temporal and spatial variations of CO_2 diffuse volcanic degassing on Cuicocha Caldera Lake – Ecuador. *Journal of Volcanology and Geothermal Research*, *411*, 107145.

Smith, E., & Dent, G. (2019). Modern Raman spectroscopy: a practical approach. John Wiley & Sons.

Stevie, F. A., & Donley, C. L. (2020). Introduction to x-ray photoelectron spectroscopy. *Journal of Vacuum & Science Technology A*, 38(6).

Subasinghe, C. S., Ratnayake, A. S., Roser, B., Sudesh, M., Wijewardhana, D. U., Attanayake, N., & Pitawala, J. (2022). Global distribution, genesis, exploitation, applications, production, and demand of industrial heavy minerals. *Arabian Journal of Geosciences*, *15*(20), 1616.

Tzifas, I. T., Misaelides, P., Godelitsas, A., Gamaletsos, P. N., Nomikou, P., Karydas, A. G., ... & Papadopoulos, A. (2017). Geochemistry of coastal sands of Eastern Mediterranean: The case of Nisyros volcanic materials. Geochemistry, 77(3), 487-501.

Unsoy, G., Gunduz, U., Oprea, O., Ficai, D., Sonmez, M., Radulescu, M., ... & Ficai, A. (2015). Magnetite: from synthesis to applications. *Current topics in medicinal chemistry*, *15*(16), 1622-1640.

Vallejo Vargas, S. X. (2011). *Distribución de las cenizas volcánicas Holocénicas Tardías en la Costa del Ecuador* [Bachelor's thesis, Escuela Politécnica Nacional].

Varela, R. (2014). *Manual de geología* [Doctoral thesis, Universidad Nacional de Tucumán].

Villagómez, D. (2003). *Evolución Geológica Plio-cuaternaria del Valle Interandino Central en Ecuador (zona de Quito-Guayllabamba-San Antonio de Pichincha)* [Undergraduate thesis, Escuela Politécnica Nacional].

Von Hillebrandt, C. (1989). *Estudio geovulcanológico del Complejo vulcanico Cuicocha-Cotacachi y sus aplicaciones, Provincia de Imbabura* [Master´s thesis, Escuela Politécnica Nacional].

Yang, S. Y., Jung, H. S., Choi, M. S., & Li, C. X. (2002). The rare earth element compositions of the Changjiang (Yangtze) and Huanghe (Yellow) river sediments. *Earth and Planetary Science Letters*, 201(2), 407-419.

Zappettini, E.O., 2022. Elementos de las tierras raras. Panorama general y evaluación del potencial en la República Argentina. Instituto de Geología y Recursos Minerales. Servicio Geológico Minero Argentino. Serie Contribuciones Técnicas. Recursos Minerales N°48, 95 pp.